Tailored nonlinear stiffness and geometric damping: applied to a bistable vibration absorber

Preprint · August 2023

DOI: 10.13140/RG.2.2.23615.69284

Kevin Dekemele
Ghent University
49 PUBLICATIONS **484** CITATIONS

Tailored nonlinear stiffness and geometric damping: applied to a bistable vibration absorber

Kevin Dekemele[a]

[a] *Ghent University, Department of Electromechanical, Systems and Metal Engineering, Tech Lane Ghent Science Park - Campus A 125, 9052, Ghent, Belgium*

Abstract

A novel device is proposed to obtain arbitrary restoring force characteristics and nonlinear geometric damping. It consists of linear springs and dampers that are compressed along a track. The obtained nonlinear damping and stiffness law depend on the track's shape. The device is then applied to obtain a nonlinear energy sink (NES) to damp the vibrations of a host system. Both the case of transient vibrations, induced by shock loads, and sustained vibrations, induced by harmonic loads, are studied. For arbitrary stiffness and damping, slow flow dynamics and slow invariant manifolds (SIMs) are derived by applying harmonic balancing and multiple timescales techniques. Under transient vibrations, two performance measures are derived from the SIM, the relative residual energy and the pumping time, and are found for generic nonlinear spring force and nonlinear geometric damping. For sustained vibrations, a load-dependent frequency response (FR) is derived from the SIMs. This FR predicts the occurrence of the efficient strongly modulated responses but also the occurrence of the unfavorable detached responses called isolas, where the NES fails to mitigate and even amplifies vibrations.

This research investigates the performance of a conventional cubic NES and a bistable NES (BNES) with nonlinear damping obtained from the proposed device. Especially the BNES with nonlinear damping shows attractive properties, with a high degree of robustness over a wide energy range and a low vibration threshold under transient loading. Under harmonic loads, the nonlinear damping helps reduce the effect of isolas. A novel tuning methodology is proposed to avoid isolas for a range of load magnitudes. The new device opens up a whole range of possibilities regarding energy dissipation through nonlinear damping.

Keywords: Nonlinear damping, Passive Vibration Control, Dynamic Vibration Absorber, Nonlinear Energy Sink, Bistable stiffness

---

1. Introduction

In the field of passive vibration control, tuned-mass-dampers (TMD) are by far the most investigated and implemented devices. It consists of a linear mass-spring oscillator with linear viscous damping to dissipate energy [1]. An efficient TMD design implies matching the TMD's natural frequency to the harmful vibration frequency of the host system it is meant to protect. However, the TMD's effective frequency range is relatively small, and a shift or uncertainty in vibration frequency or the presence of multiple vibration modes limits the TMD's effectiveness. Multiple TMDs can be added to address the issues mentioned above [2, 3].

In the last 20 years, a vibration control device with a strongly nonlinear restoring force called the nonlinear energy sink (NES) has been proposed [4, 5, 6] The strongly nonlinear restoring force enables an amplitude-dependant natural frequency, unlike linear TMDs, which have a fixed natural frequency. As such, the NES can self-tune itself to the vibration frequency of its host system. As an effect, it has a larger frequency bandwidth than the TMD, which is only effective around its fixed natural frequency.

The NES has been investigated for different types of loading as transient [7, 8], harmonic [9, 10, 11] and stochastic loading [12, 13]. The conventional NES has a polynomial hardening restoring force, typically purely cubic. However, other restoring forces have been proposed as bistable [14, 15, 16, 17, 18], softening [19], hardening-softening [13, 20], periodic [21] or impact [22, 23, 24]. The above works study the effect of shock loads or harmonic loads on the host system, while the performance of the NES under self-sustained oscillations has also been studied [25, 26, 27]. In many works, it is shown that the conventional NES has a limited efficient energy range. A too-low or too-high forcing or input energy at the main structure side renders the NES inefficient. On the low energy side, the NES does not dissipate significantly unless a certain level of vibration energy, or energy threshold, is present in the host system. Just above the energy threshold, the NES performs efficiently. However, as the vibration energy increases to higher levels, the performance also decreases. Furthermore, under transient loading, the conventional NES fails to dissipate all the energy, leaving a residual amount of vibration energy in the host system. To lower the energy threshold and reduce residual energy, an NES with bistable stiffness can be used [18]. However, the decreased efficiency at higher energy levels remained, and under low energy conditions and/or high linear damping, the NES vibrated chaotically, with reduced vibration mitigation performance. A device has been proposed that increases the viscous damping of the conventional cubic NES with the vibration amplitude [28, 29, 30, 31]. The proposed nonlinear damping coefficient was approximately

---

[*] Corresponding Author

Email address: `kevin.dekemele@ugent.be` (Kevin Dekemele) proportional to the square of the displacement, $c_{\mathrm{gd}}(z) = z^2$, where the damping force is $z^2\dot{z}$. This type of damping, where the damping depends on the position, is called geometric damping. This damping increases the NES performance for high energy levels. Furthermore, under harmonic excitations, the nonlinear geometric damping can even reduce the effects of the undesired detached resonance curves, called isolas [32, 33]. Other nonlinear damping forces have been proposed that are nonlinear in the speed [33, 34, 35], e.g., $c_{\mathrm{gd}}(z) = \dot{z}^2$ or increasing and then decreasing with the displacement [36]. The current research will tackle all downsides of the conventional NES by combining a bistable restoring force and a nonlinear geometric damping. Bistable restoring forces can be obtained in several ways, by using pre-stressed springs or beams perpendicular to the stroke of the NES [37, 38, 15], an array of magnets [16, 39, 40] or by constraining linear springs to a nonlinear machined track [41, 42, 43]. The latter method will be used here; in particular, an enhancement of the device in [41] is proposed to include the option to tailor the nonlinear geometric damping by fitting a linear damper that follows the nonlinear machined track. It will be shown that the nonlinear geometric damping obtained using the same track as for the desired restoring force is proportional to the square of the restoring force divided by the restoring force's potential energy. Although this paper will focus on a bistable NES, the proposed device can make both arbitrary nonlinear stiffness and nonlinear geometric damping. This ability opens a whole new field of study as now nonlinear geometric damping is not only restricted to the $c_{\mathrm{gd}}(z) = z^2$ type.

A framework is developed to design, assess, and optimize the performance of NES with generic geometric damping and restoring force, for both transient vibrations under shock load and sustained vibrations under harmonic loads. Here it will be applied to the conventional cubic NES and the bistable NES, with associated nonlinear geometric damping obtained from the proposed device. In the next section, the proposed device is presented and it is shown how to tailor-make nonlinear stiffness and nonlinear damping. Section 3 presents the equations of motion of the device attached to a linear oscillator under transient load. For arbitrary stiffness and damping, slow flow dynamics and a slow invariant manifold are derived by applying harmonic balance and multiple timescales techniques. Then, in section 4, the slow flow performance measures are presented, which allows to efficiently compute the dissipation rate and residual energy for arbitrary damping and stiffness. From then on, the particular case of hardening and bistable stiffness is investigated with their corresponding nonlinear geometric damping. Section 5 presents numerical performance and an optimization method based on the full equations of motions. Sections 6 and 7 investigate the behavior of the NES under harmonic loads through harmonic balancing, and a novel tuning scheme is proposed to avoid isolas. Finally, the conclusions are presented.

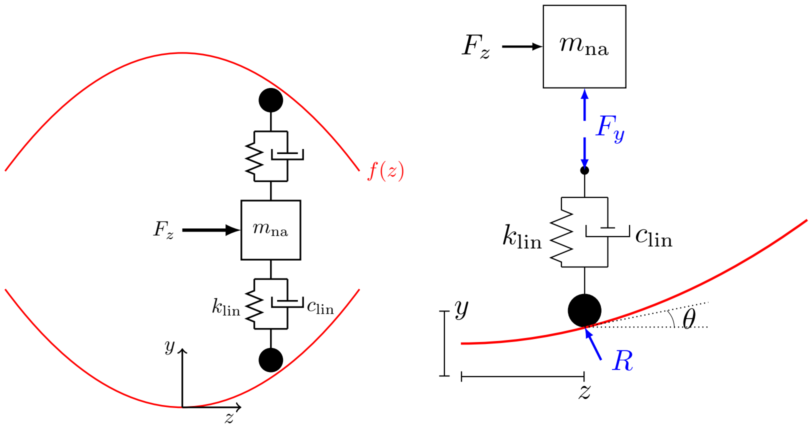

(a) (b)

Figure 1: The proposed device to obtain nonlinear stiffness and nonlinear geometric. The mass moves horizontally, and the linear springs and dampers k_{lin} and c_{lin} are compressed according to track $f(z)$, (a) is an overview and (b) a closer look at the internal forces.

2. Proposed device

Figure 1a shows a scheme of the proposed device. It consists of a mass m_{na} moving in the z-direction. Linear springs and dampers c_{lin} and k_{lin} are attached to the mass and their other ends are connected with a follower. The follower can move along a track $f(z)$. As the mass moves horizontally due to an applied time-varying force $F_z(t)$, the spring and damper are compressed according to the track $f(z)$. This causes the reaction forces F_y and R as depicted in Figure 1b. The reaction forces and applied force are related as follows:

$$F_z = 2R\sin(\theta) \quad F_y = R\cos(\theta) \Rightarrow F_z = 2F_y\tan(\theta) \tag{1}$$

with $\theta(x)$ is the slope angle of $f(z)$, related to the track by $\tan\theta = \frac{df(z)}{dz}$. The follower end is compressed by $y = f(z)$ and has velocity $\dot{y} = \dot{f}(z) = \frac{df(z)}{dz}\dot{z}$. The reaction force F_y is thus:

$$F_y = k_{\text{lin}} f(z) + c_{\text{lin}}\frac{df(z)}{dz}\dot{z} \tag{2}$$

where $\dot{}$ stand for time derivative $\frac{d}{dt}$. Finally, combining the equations (1) and (2) yields the relation between the applied force and the track:

$$F_z = \underbrace{2k_{\text{lin}} f(z) \frac{df(z)}{dz}}_{F_{\text{s}}} + \underbrace{2c_{\text{lin}} \left(\frac{df(z)}{dz} \right)^2 \dot{z}}_{F_{\text{gd}}} \tag{3}$$

where F_{s} is the obtained spring force and F_{gd} is the obtained geometric damping. It is called geometric damping, as the nonlinearity depends only on the displacement.

In [41, 42], the track $f(z)$ was designed to tailor a predetermined spring characteristic $F_{\text{s}}(z)$. The relation between the desired spring force and the track is:

$$\frac{df(z)}{dz} = \frac{F_{\text{s}}}{2f(z)k_{\text{lin}}} \Rightarrow f(z) = \sqrt{\frac{1}{k_{\text{lin}}} \int_0^z F_{\text{s}}(z)dz + f(0)^2} \tag{4}$$

where $f(0)$ is the pre-stress of the spring k_{lin} at $z = 0$. As such, $\frac{df(z)}{dz}$ is:

$$\frac{df(z)}{dz} = \frac{1}{k_{\text{lin}}} \frac{F_{\text{s}}(z)}{2\sqrt{\frac{1}{k_{\text{lin}}} \int_0^z F_{\text{s}}(z)dz + f(0)^2}} \tag{5}$$

The associated geometric damping force for this track is then:

$$F_{\text{gd}} = \underbrace{\frac{c_{\text{lin}}}{2k_{\text{lin}}} \frac{F_{\text{s}}^2(z)}{\int_0^z F_{\text{s}}(z)dz + k_{\text{lin}} f(0)^2}}_{c_{\text{gd}}(z)} \dot{z} \tag{6}$$

where c_{gd} is the geometric damping coefficient, that depends on the displacement in a nonlinear way.

In this paper, the stiffnesses under investigation are the conventional hardening cubic and the bistable stiffness. The required tracks are, respectively:

$$\begin{aligned} F_{\text{s}} &= k_3 z^3 && \Rightarrow && f(z) = \frac{1}{2}\sqrt{\frac{k_3}{k_{\text{lin}}}} z^2 \\ F_{\text{s}} &= k_3 z^3 - k_1 z && \Rightarrow && f(z) = \sqrt{\frac{1}{k_{\text{lin}}} \left(\frac{k_3}{4} z^4 - \frac{k_1}{2} z^2 \right) + f(0)^2} \end{aligned} \tag{7}$$

For the cubic stiffness, it is opted for no pre-stress, $f(0) = 0$. For the bistable stiffness, the pre-stress should make the terms under the square root positive for

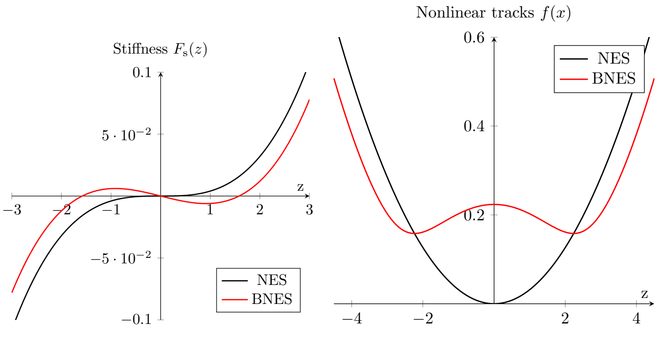

(a) (b)

Figure 2: The NES and BNES stiffness (a) and required track (b) for $F_\mathrm{s} = 0.004z^3$ for the NES and $F_\mathrm{s} = 0.004z^3 - 0.01z$ for the BNES, and $k_\mathrm{lin} = 1$ and pre-stress of $f(0) = 0$ for the NES and $f(0) = \sqrt{0.05}$ for the BNES.

all z, $f(0)^2 > \frac{1}{k_\mathrm{lin}} \left(\frac{k_3}{4} z^4 - \frac{k_1}{2} z^2 \right)$.
The associated nonlinear geometric damping forces for these two types of stiffnesses are:

$$\begin{aligned}
F_\mathrm{s} &= k_3 z^3 && \Rightarrow \quad F_\mathrm{gd} = \underbrace{\frac{c_\mathrm{lin}}{2k_\mathrm{lin}} 4k_3 z^2}_{c_\mathrm{gd}(z)} \dot{z} \\
F_\mathrm{s} &= k_3 z^3 - k_1 z && \Rightarrow \quad F_\mathrm{gd} = \underbrace{\frac{c_\mathrm{lin}}{2k_\mathrm{lin}} \frac{\left(k_3 z^3 - k_1 z\right)^2}{\frac{k_3}{4} z^4 - \frac{k_1}{2} z^2 + k_\mathrm{lin} f(0)^2}}_{c_\mathrm{gd}(z)} \dot{z}
\end{aligned} \tag{8}$$

The track for an NES where $F_\mathrm{s} = 0.004z^3$ and a BNES where $F_\mathrm{s} = 0.004z^3 - 0.01z$ is shown on Figure 2. The stiffness forces in Figure 2a have their corresponding track in Figure 2b. A stiffness $k_\mathrm{lin} = 1$ and pre-stress of $f(0) = \sqrt{0.05}$ (only for the BNES) was used to compute the tracks. Figure 3 plots the associated nonlinear damping coefficient where $c_\mathrm{lin} = 1$. For small z, Figure 3a, the damping of the BNES is much smaller and even is zero for $z = \pm\sqrt{\frac{k_1}{k3}}$, the exact point where the stiffness force is zero as well, Figure 2a. These two points are also the stable points. For increasing z, the damping coefficient for the BNES approaches the NES's, Figure 3b.

Remark. The nonlinear geometric damping can also be tailored to a desired damping force $F_\mathrm{gd} = c_\mathrm{gd}(z)\dot{z}$. Manipulating the damping force (3) yields:

$$\frac{df(z)}{dz} = \sqrt{\frac{c_\mathrm{gd}(z)}{2c_\mathrm{lin}}} \Rightarrow f(z) = \sqrt{\frac{1}{2c_\mathrm{lin}}} \int_0^z \sqrt{c_\mathrm{gd}(z)} dz + f(0) \tag{9}$$

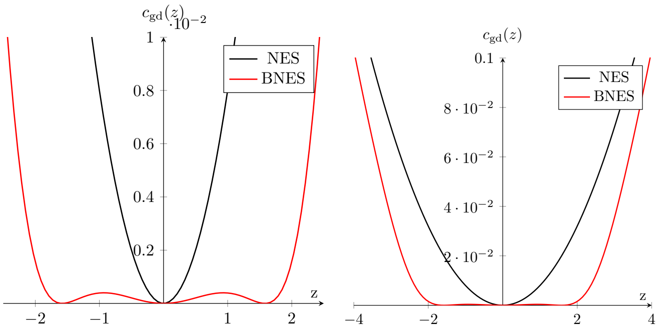

(a) (b)

Figure 3: The geometric damping, (7), for the NES and BNES associated with the tracks found in Figure 2b, where for the NES (black line) $k_3 = 0.004$ for the BNES (red) $k_3 = 0.004$, $k_1 = 0.01$ and $f(0) = \sqrt{0.05}$. For both NESs, $k_{\mathrm{lin}} = 1$ and $c_{\mathrm{lin}} = 1$. (a) and (b) represent the same functions both for other ranges.

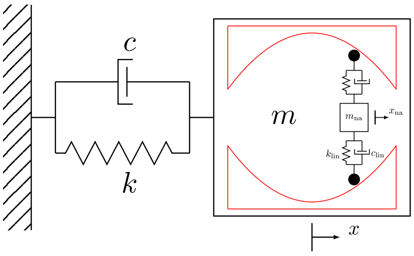

Figure 4: A 1DOF host system fitted with proposed NES.

The associated nonlinear stiffness is then:

$$F_{\mathrm{s}} = 2k_{\mathrm{lin}}\sqrt{\frac{c_{\mathrm{gd}}(z)}{2c_{\mathrm{lin}}}}\left(\sqrt{\frac{1}{2c_{\mathrm{lin}}}}\int_0^z \sqrt{c_{\mathrm{gd}}(z)}dz + f(0)\right) \tag{10}$$

Additionally, in an extension of the proposed device, the linear spring and damping of the device can be connected to separate tracks, allowing both tailoring damping and stiffness independently.

3. Dynamics of nonlinear energy sink attached to linear oscillator

3.1. Equations of motion

The proposed device is attached to a linear oscillator (LO) host system. A scheme of this configuration is shown in Figure 4. The nonlinear track in red is fixed to the host system's mass. The equations of motion (EOM) are:

$$
\begin{aligned}
&m\ddot{x} + c\dot{x} + kx + c_{\mathrm{na}}(\dot{x} - \dot{x}_{\mathrm{na}}) + c_{\mathrm{gd}}(x - x_{\mathrm{na}})(\dot{x} - \dot{x}_{\mathrm{na}}) + F_{\mathrm{s}}(x - x_{\mathrm{na}}) = 0 \\
&m_{\mathrm{na}}\ddot{x}_{\mathrm{na}} - c_{\mathrm{na}}(\dot{x} - \dot{x}_{\mathrm{na}}) - c_{\mathrm{gd}}(x - x_{\mathrm{na}})(\dot{x} - \dot{x}_{\mathrm{na}}) - F_{\mathrm{s}}(x - x_{\mathrm{na}}) = 0
\end{aligned}
\tag{11}
$$

where m, k, c are the host system's mass, spring and damping, m_{na} and c_{na} are the NES mass and linear damping. The nonlinear spring force F_{s} and nonlinear geometric damping c_{gd} are determined by the track of the device. After some rearrangements, dividing by m, introducing dimensionless time $\tau = \sqrt{\frac{k}{m}}t = \omega_{\mathrm{n}}t$ and relative absorber coordinate $z = x_{\mathrm{na}} - x$, equation (11) is written in dimensionless coefficients:

$$
\begin{aligned}
&x'' + \varepsilon\xi x' + x + \varepsilon\left(z'' + x''\right) = 0 \\
&\varepsilon\left(z'' + x''\right) + \varepsilon\xi_{na}z' + \varepsilon\xi_{\mathrm{gd}}(z)z' + \varepsilon f_{\mathrm{s}}(z) = 0
\end{aligned}
\tag{12}
$$

where $'$ is the time derivative w.r.t. τ and:

$$
\varepsilon = \frac{m_{\mathrm{na}}}{m} \quad \xi = \frac{c}{m_{\mathrm{na}}\omega_{\mathrm{n}}} \quad \xi_{\mathrm{na}} = \frac{c_{\mathrm{na}}}{m_{\mathrm{na}}\omega_{\mathrm{n}}} \quad \xi_{\mathrm{gd}}(z) = \frac{c_{\mathrm{gd}}(z)}{m_{\mathrm{na}}\omega_{\mathrm{n}}} \quad f_{\mathrm{s}}(z) = \frac{F_{\mathrm{s}}(z)}{m_{na}\omega_n^2}
\tag{13}
$$

with ε the mass ratio, assumed small ($\varepsilon \ll 1$), and ξ and ξ_{na} dimensionless damping constants. Although the cubic and bistable stiffness will be studied in later sections, the general forms of stiffness $f_{\mathrm{s}}(\cdot)$ and nonlinear damping $c_{\mathrm{gd}}(\cdot)$ will be kept in this section to keep the analysis generic. For the spring forces of the conventional NES and bistable NES, f_{s} is:

$$
F_{\mathrm{s}} = k_3 z^3 \Rightarrow f_s = \gamma z^3, \quad F_{\mathrm{s}} = k_3 z^3 - k_1 z \Rightarrow f_s = \gamma z^3 - \kappa z
\tag{14}
$$

where

$$
\gamma = \frac{k_3}{m_{\mathrm{na}}\omega_n^2} \quad \kappa = \frac{k_1}{m_{\mathrm{na}}\omega_n^2}
\tag{15}
$$

where κ is the dimensionless negative stiffness coefficient and γ the nonlinear stiffness coefficient. The latter has dimension $[1/\mathrm{m}^2]$. Later on, γ is used to nondimensionalize the displacement, but for now, the analysis is kept for a generic nonlinear spring force. The nonlinear geometric damping of (8) be expressed in κ and γ:

$$
\begin{aligned}
&F_{\mathrm{s}}(z) = k_3 z^3 && \Rightarrow \xi_{\mathrm{gd}}(z) = 2\omega_{\mathrm{n}}\frac{c_{\mathrm{lin}}}{k_{\mathrm{lin}}}\frac{k_3}{m_{\mathrm{na}}\omega_{\mathrm{n}}^2}z^2 = \tilde{\xi}_{\mathrm{gd}}\gamma z^2 \\
&F_{\mathrm{s}}(z) = k_3 z^3 - k_1 z && \Rightarrow \xi_{\mathrm{gd}}(z) = \frac{\tilde{\xi}_{\mathrm{gd}}}{4}\gamma z^2 \frac{\left(\gamma z^2 - \kappa\right)^2}{\frac{\gamma^2}{4}z^4 - \frac{\kappa\gamma}{2}z^2 + \tilde{f}(0)^2}
\end{aligned}
\tag{16}
$$

where $\tilde{\xi}_{\mathrm{gd}} = 2\omega_{\mathrm{n}}\frac{c_{\mathrm{lin}}}{k_{\mathrm{lin}}}$ and $\tilde{f}(0)^2 = \frac{k_{\mathrm{lin}}f(0)^2\gamma^2}{k_3}$.

3.2. Slow flow dynamics of 1:1 resonance

To better understand the NES performance, a slow flow manifold will now be derived from the EOM. For this, a 1:1 resonance harmonic balancing (HB) and a two timescales scheme is applied. In this context, 1:1 resonance implies that both the NES and LO vibrate with the same, single, frequency. The first step in the approach is complexifing x and z to complex variables of Manevitch $A, B \in \mathbb{C}$ [44]:

$$2A(\tau)e^{i\tau} = x - ix' \quad 2B(\tau)e^{i\tau} = z - iz' \tag{17}$$

where the original variables are then substituted by:

$$\begin{aligned} x &= A(\tau)e^{i\tau} + A^*(\tau)e^{-i\tau} & z &= B(\tau)e^{i\tau} + B^*(\tau)e^{-i\tau} \\ x' &= iA(\tau)e^{i\tau} - iA^*(\tau)e^{-i\tau} & z' &= iB(\tau)e^{i\tau} - iB^*(\tau)e^{-i\tau} \end{aligned} \tag{18}$$

where * indicates the complex conjugate. Deriving $2A(\tau)e^{i\tau} = x - ix'$ and $2B(\tau)e^{i\tau} = z - iz'$ yields after some manipulations:

$$x'' + x = i2A'e^{i\tau} \quad z'' + z = i2B'e^{i\tau} \tag{19}$$

Then, after substituting equations (18) and (19) in the EOM (12), only the terms that are multiplied by $e^{-i\tau}$ are kept. This is a consequence of the 1:1 resonance assumption. Then,dividing by $e^{-i\tau}$ yields: :

$$\begin{aligned} &2A' + \varepsilon\xi A + \varepsilon(2B' + iB + 2A'_h + iA) = 0 \\ &2B' + iB + 2A' + iA + \xi_{\mathrm{na}}B - iBG(B, B^*) + BH(B, B^*) = 0 \end{aligned} \tag{20}$$

The terms $G(B, B^*)$ and $H(B, B^*)$ are obtained from a modified Galerkin method, that comes down to projecting the nonlinear forces on the first harmonic of a truncated Fourier series [45, 46]

$$\begin{aligned} BG(B, B^*) &= \frac{1}{2\pi}\int_0^{2\pi} f_{\mathrm{s}}\left(Be^{i\tau} + B^*e^{-i\tau}\right)e^{-i\tau}d\tau \\ BH(B, B^*) &= \frac{1}{2\pi}\int_0^{2\pi} \xi_{\mathrm{gd}}\left(Be^{i\tau} + B^*e^{-i\tau}\right)\left(Be^{i\tau} - B^*e^{-i\tau}\right)e^{-i\tau}d\tau \end{aligned} \tag{21}$$

In Appendix A, the procedure to compute these integrals is explained. In [47], it was shown that H and G only depend on the modulus of B, $G(|B|)$ and $H(|B|)$. Then, the dynamics in (20) are regarded as acting in two timescales, a fast time

τ_0 and a slow time τ_1:

$$A(\tau) = A_h(\tau_0, \tau_1), \quad B(\tau) = B(\tau_0, \tau_1), \quad \tau_0 = \tau,\, \tau_1 = \varepsilon\tau \quad , \frac{d}{d\tau} = \frac{\partial}{\partial \tau_0} + \varepsilon \frac{\partial}{\partial \tau_1} \tag{22}$$

By applying this procedure to (20) and collecting terms according to their order in ε, the following is obtained:

$$\begin{aligned} &\frac{\partial A}{\partial \tau_0} = 0 \\ &2\frac{\partial A}{\partial \tau_1} + \xi A + 2\frac{\partial B}{\partial \tau_0} + iB + 2\cancel{\frac{\partial A}{\partial \tau_0}} + iA = 0 \\ &2\frac{\partial B}{\partial \tau_0} + iB + 2\cancel{\frac{\partial A}{\partial \tau_0}} + iA + \xi_{\mathrm{na}} B - iBG(|B|) + BH(|B|) = 0 \end{aligned} \tag{23}$$

The complex A and B written in polar form are $A = ae^{i\alpha}/2$ and $B = be^{i\beta}/2$. The equations (23) in polar form are split into their real and imaginary parts, resulting in the following set of equations:

$$\begin{aligned} &2\frac{\partial a}{\partial \tau_1} = -\xi a + b\sin(\beta - \alpha), \quad 2a\frac{\partial \alpha}{\partial \tau_1} = -b\cos(\beta - \alpha) - a \\ &\xi_{\mathrm{na}} b + bH(b) = -a\sin(\beta - \alpha), \quad b - bG\,(b) = -a\cos(\beta - \alpha) \end{aligned} \tag{24}$$

Subsequently, a new equation is obtained by inserting the third into the first equations of (24), and a another equation by squaring and adding the third and fourth equations:

$$\begin{aligned} &\frac{\partial a^2}{\partial \tau_1} = -\xi a^2 - \xi_{\mathrm{na}} b^2 - b^2 H(b) \\ &a^2 = b^2 \left((\xi_{\mathrm{na}} + H(b))^2 + (1 - G(b))^2 \right) \end{aligned} \tag{25}$$

The first equation describes the dynamics of the slow flow and the second is the slow invariant manifold (SIM), i.e., a static relation between a en b where dynamics are confined to.

The stability computation of the SIM is presented in Appendix B. The SIM, the slow flow dynamics and its stability that were just derived, hold for any restoring force F_{s} and geometric damping c_{gd}. Here, $G(b)$ and $H(b)$ for the restoring force in (14) are computed in Appendix A. For the studied restoring forces and geometric damping, the displacements can also be dimensionless, where

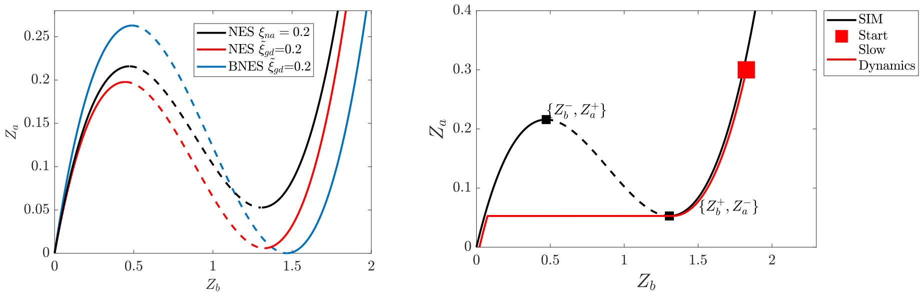

(a)

(b)

Figure 5: (a) Collection of SIMs, for an NES with linear damping $\xi_{\text{na}} = 0.2$ (black), an NES with nonlinear geometric damping $\tilde{\xi}_{\text{gd}} = 0.2$ (red) and a BNES with $\tilde{\xi}_{\text{gd}} = 0.2$, $\kappa = 0.1$ and $\tilde{f}(0) = 1$. (b) Visualization of the slow dynamics (red) on the SIM (black) for an NES where $\xi_{\text{na}} = 0.2$ and $\kappa = \tilde{\xi}_{\text{gd}} = 0$. In both Figures, the dashed lines are unstable solutions.

$Z_a = \gamma a^2$ and $Z_b = \gamma b^2$:

$$\begin{aligned} \frac{\partial Z_a}{\partial \tau_1} &= -\xi Z_a - \xi_{\text{na}} Z_b - \tilde{\xi}_{\text{gd}} Z_b \tilde{H}(Z_b) \\ Z_a &= Z_b \left(\left(\xi_{\text{na}} + \tilde{\xi}_{\text{gd}} \tilde{H}(Z_b) \right)^2 + (1 - G(Z_b))^2 \right) \end{aligned} \tag{26}$$

where

$$\begin{aligned} \text{NES} \Rightarrow \tilde{H}(b) &= \frac{Z_b}{4} \\ \text{BNES} \Rightarrow \tilde{H}(b) &= \frac{Z_b}{8\pi} \int_0^{2\pi} \frac{\left(Z_b \cos^2(\tau_\beta) - \kappa \right)^2}{\frac{Z_b^2}{4} \cos^4(\tau_\beta) - \frac{\kappa Z_b}{2} \cos^2(\tau_\beta) + \tilde{f}(0)^2} \sin^2(2\tau_\beta) d\tau_\beta \end{aligned} \tag{27}$$

The SIMs for the conventional NES with linear damping ($\xi_{\text{na}} = 0.2$, $\tilde{\xi}_{\text{gd}} = 0$), the conventional NES with geometric damping ($\xi_{\text{na}} = 0$, $\tilde{\xi}_{\text{gd}} = 0.2$) and BNES with geometric damping ($\xi_{\text{na}} = 0$, $\tilde{\xi}_{\text{gd}} = 0.2$, $\kappa = 0.1$ and $\tilde{f}(0)^2 = 1$ are visualized in Figure 5a. All SIMs have the same S-shape, with a stable left branch, an unstable middle branch and a stable right branch. When the slow flow is initially on the right branch, Z_b is large, and as such, so is $\frac{\partial Z_a}{\partial \tau_1}$ (26). Then, targeted energy transfer (TET) happens, where most energy is transferred to the NES and is dissipated by the NES.

In the next section, the equations in (26) are used to derive slow flow performance measures.

4. Slow flow performance measures

Under the efficient TET regime, the dynamics in the slow flow initiate in $\{Z_b(0), Z_a(0)\}$ on the rightmost branch on the SIM. Figure 5b visualizes TET. The first equation in (26) dictates that Z_a should decrease (negative derivative). When the dynamics are on the right branch, Z_a can decrease up until the local minimum $\{Z_b^+, Z_a^-\}$. At this point, the slow flow jumps to the left branch, where low Z_b indicates bad NES performance as then the $\frac{\partial Z_a}{\partial \tau_1}$ is small. For the conventional NES, it was shown that attraction to the right branch was ensured when the initial $Z_a(0)$ in the LO is above an energy threshold that corresponded with the maximum of the SIM, $Z_a(0) > Z_a^+$ [7], while for the BNES this was not required, and a lower threshold was found [18], slightly above Z_a^- From a performance point of view, the descent of the SIM should happen quickly and the amount of energy dissipated should be high. Two performance measures can be computed to express this, the relative residual energy and the pumping time.

4.1. Relative residual energy

Once the slow flow has jumped to the left branch, an amount of residual energy, mainly in the host system, dissipates slowly. Relative to the initial energy in the host system, the residual energy in the host system is defined as:

$$E_{\text{res}} = \frac{Z_a^-}{Z_a(0)} \tag{28}$$

where $Z_a(0) = \gamma a(0)^2 = \gamma\sqrt{x(0)^2 + x'(0)^2}$.

4.2. Pumping time

The time to descend the SIM from an initial point to the local minimum can be computed by combining the slow flow dynamics and SIM in equation (25) and integrating after separation of variables τ_1 and Z_b [7, 18, 41, 37, 10]. The first step is to compute $\partial Z_a / \partial Z_b$ by deriving the SIM:

$$\begin{aligned} \frac{\partial Z_a}{\partial Z_b}(Z_b) = {} & 2\tilde{\xi}_{\text{gd}} Z_b \frac{\partial \tilde{H}(Z_b)}{\partial Z_b}\left(\xi_a + \tilde{\xi}_{\text{gd}}\tilde{H}(Z_b)\right) + 2Z_b\gamma\frac{\partial G(Z_b)}{\partial Z_b}\left(G(Z_b) - 1\right) \\ & + \left(\left(\xi_{\text{na}} + \tilde{\xi}_{\text{gd}}\tilde{H}(Z_b)\right)^2 + \left(1 - G(Z_b)\right)^2\right) \end{aligned} \tag{29}$$

Equating this expression to zero can also be used to compute the extrema $\{Z_b^-, Z_a^+\}$ and $\{Z_b^+, Z_a^-\}$ of the SIM. Then, $\partial Z_b / \partial \tau_1$ is obtained from:

$$\frac{\partial Z_b}{\partial \tau_1} = \frac{\partial Z_a}{\partial \tau_1}\frac{\partial Z_b}{\partial Z_a} = \frac{-\xi^2 Z_a - \xi_{\text{na}} Z_b - \tilde{\xi}_{\text{gd}} Z_b \tilde{H}(Z_b)}{\frac{\partial Z_a}{\partial Z_b}} \tag{30}$$

Then, separation of variables and integration yields:

$$\int_{Z_b(0)}^{Z_b^+} \frac{\frac{\partial Z_a}{\partial Z_b}(Z_b)}{-\xi Z_a - \xi_{\mathrm{na}} Z_b - \tilde{\xi}_{\mathrm{gd}} Z_b \tilde{H}(Z_b)} \partial Z_b = \tau_{1,\mathrm{pump}} = \varepsilon T_{\mathrm{pump}} \tag{31}$$

where $\tau_{1,\mathrm{pump}}$ is the pumping time in slow time, and T_{pump} in fast time. It is opted to express the pumping time in the fast time in the rest of the paper. The solution of this integral for the conventional NES was presented in [7]. For the NES with geometric damping, $\tilde{H}(Z_b) = \frac{Z_b}{4}$, the integral can be solved analytically using mathCAD software as Wolfram Mathematica. For example, for $\xi = \xi_{\mathrm{na}} = 0$, the pumping time is:

$$\varepsilon T_{\mathrm{pump}} = \left[\frac{4\left(3\ln\left(|Z_b|\right) - \frac{\left(3\xi_{\mathrm{gd}}^2 + 27\right) Z_b}{16} + \frac{1}{Z_b}\right)}{\xi_{\mathrm{gd}}} \right]_{Z_b(0)}^{Z_b^+} \tag{32}$$

For the BNES with nonlinear damping, this integral can not be solved analytically but can be evaluated by either numerical integration or by a Taylor series approximation of the damping.

4.3. Example

These measures are now computed for a conventional NES (= purely cubic stiffness) where $\xi_{\mathrm{na}} = 0.13$, a conventional NES with geometric damping where $\tilde{\xi}_{\mathrm{gd}} = 0.4$, a BNES where $\xi_{\mathrm{na}} = 0.11$ and $\kappa = 0.5$, and a BNES with geometric damping where $\tilde{\xi}_{\mathrm{gd}} = 1.14$, $\kappa = 0.5$ and $\tilde{f}^2(0) = 0.5$. For all configurations, $\xi = 0$. The damping coefficients of the four NESs where chosen such that $E_{\mathrm{res}} = 0.1$ for $Z_{\mathrm{a}}(0) = 0.202$, implying the same Z_{a}^-. For convenience, these NESs will be referred to as NES #1, NES #2, NES #3, NES #4, respectively.

The SIMs for these NESs are shown in Figure 6a. For NES #1 and #2, the conventional NES with linear and nonlinear damping, the energy threshold is the local maximum, where $Z_{\mathrm{a}}^+ = 0.202$. This value is computed by finding the maximum of the SIM in (26). The initial $Z_{\mathrm{a}}(0)$ should be larger than the threshold for TET to occur for NES #1 and #2 [7, 10]. The BNES, NES #3 and #4, do not have the threshold at Z_{a}^+, but at slightly above Z_{a}^- [18, 38, 37]. The residual energy and pumping time in the interval $Z_a(0) = [0.202, 5]$ is shown in Figures 6b and 6c, respectively. As the relative residual energy is almost the same for all three NESs, the pumping time is the principal measure under investigation. A mass ratio $\varepsilon = 0.02$ is used to compute the pumping time. For $Z_{\mathrm{a}}(0) = 0.202$, the minimum initial energy to ensure TET for NES #1 and #2, the pumping

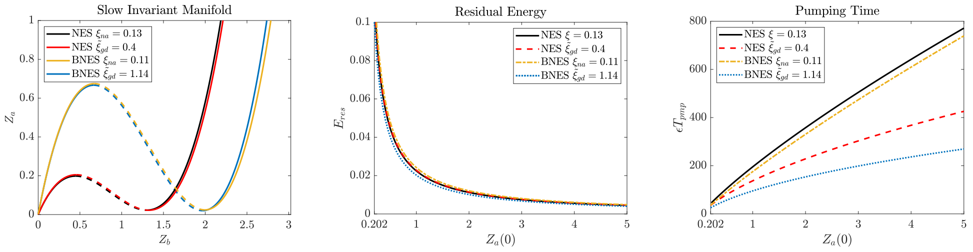

(a) (b) (c)

Figure 6: The SIMs (a), residual energy (b) and pumping time (c) for the four NESs under investigation. Where black is NES #1, red NES #2, yellow NES #3 and blue NES #4.

are 45.9 s (NES #1), 38 s (NES #2), 38.8 s (NES #3) and 27 s (NES #4), for $Z_\mathrm{a}(0) = 1$, 195 s, 137 s, 175 s and 95 s and for $Z_\mathrm{a}(0) = 5$, 771 s, 426 s, 740 s, and 269 s. Over the whole considered energy range, the pumping increases by almost 17 times for NES #1, 11% times for NES #2 and 19 times for NES #3 and 10 times for NES #4. The NES #4, the BNES with nonlinear damping, is not only faster (= lower pumping time) over the whole range, but its performance also does not decrease at the same rate as the other NESs. Next, to evaluate the viability of the performance measures of the slow flow, they will be compared to full numerical simulations through the Runga-Kutta scheme of ODE 45 in MATLAB.

4.4. Validity of slow flow performance measures

The performance measures discussed in the previous section are obtained by manipulating the slow flow dynamical equations and SIM. The complete EOM (12) for NES #1-#4 are now simulated for a shock load equivalent to $Z_a(0) = [0.202, 1, 5]$ and NES performance is compared to the slow flow performance measures. The EOM (12) are further manipulated by replacing f_s with (14) and by introducing the dimensionless displacements $\bar{x} = \sqrt{\gamma}x$ and $\bar{z} = \sqrt{\gamma}z$:

$$\begin{aligned} \bar{x}'' + \varepsilon\xi\bar{x}' + \bar{x} + \varepsilon\left(\bar{z}'' + \bar{x}''\right) = 0 \\ \varepsilon\left(\bar{z}'' + \bar{x}''\right) + \varepsilon\xi_{na}\bar{z}' + \varepsilon\xi_{\mathrm{gd}}(\bar{z})\bar{z}' + \bar{z}^3 - \kappa\bar{z} = 0 \end{aligned} \tag{33}$$

The initial conditions on (33) are computed as $Z_a(0) = (\bar{x}(0)^2 + \bar{x}'(0)^2)$. To obtain a kind of Z_a and Z_b for the complete EOM, $Z_a(\tau) = (\bar{x}(\tau)^2 + \bar{x}'(\tau)^2)$ and $Z_b(\tau) = (\bar{z}(\tau)^2 + \bar{z}'(\tau)^2)$ are computed after each simulation. The results of the simulations are presented in Figure 7. For $Z_a(0) = 0.202$, the envelope of the LO and phase plane of Z_a and Z_b with the SIMs are shown in Figures 7a and 7d. N Similarly, the envelopes and phase planes for $Z_a(0) = 1$ are found in Figures 7b and 7e and for $Z_a(0) = 5$ in Figures 7c and 7f. ES #3 is not shown on these last 4 figures as not to overload them, as the same curves as NES #4 (blue) is followed.

The time where Z_a of the full EOM crosses $Z_a^- = 0.0202$, indicated by the colored squares on the figures, is defined here as 'fast pumping time' $T_{\text{pump,f}}$:

$$T_{\text{pump,f}} = \{\tau : Z_a(\tau) = (\bar{x}(\tau)^2 + \bar{x}'(\tau)^2) = Z_a^-\} \tag{34}$$

This is compared to the pumping time computed from the slow flow in Table 1. Here, the relative difference $\Delta\%$ between the fast and slow pumping time is computed as:

$$\Delta\% = \frac{T_{\text{pump,f}} - T_{\text{pump}}}{T_{\text{pump,f}}} \tag{35}$$

For $Z_a(0) = 0.2020$, the slow flow pumping time underestimates the fast pumping time fo for the conventional NESs (#1 and#2), and slightly overestimates the fast pumping time for the BNESs (#3 and#4). As the energy increases, the slow flow pumping time for NES #1 gets closer to fast pumping time while for the NES other (NES #2-#4) slow flow pumping time becomes quite an overestimation, especially the NESs with nonlinear geometric damping. For even higher initial energies, this would also be the case for NES #1 [48]. The reason for the faster pumping time for the full EOM is the presence of higher harmonics, see for example, the wavelet transform of $\bar{z}$ for NES #4 for $Z_a(0) = 5$ in Figure 8. Only vibrations with frequency ω_n were considered when deriving the slow flow dynamics, which explains the incorrectly estimated slow flow pumping time when other (higher) harmonics are present. As such, the presence of these higher harmonics hastens the dissipation because these increase the damping forces, which depend on the speed, significantly. The slow flow pumping time can still serve as a qualitative comparison between NESs rather than a quantitative performance measure to measure the absolute dissipation time.

However, the computation of (31) assumes the existence of the SIM minimum, Z_b^+, which requires the S-shaped structure of the SIM. This is not always the case depending on the coefficients [17, 21]. For this reason, and the fact that the pumping time is not correctly estimated for larger energies, the next section presents a numerical optimization scheme for the full EOM to quantify the performance over the whole parameter space correctly.

Finally, to verify that $Z_a(0) > Z_a^+$ is the energy threshold for the conventional NESs, but not the BNESs, the full EOM is simulated for $Z_a(0) = 0.18 < Z_a^+$. The results are shown in Figure 9. The envelopes in Figure 9a show that the conventional NES with linear and nonlinear damping fail in TET, while the BNESs succeeds. The reason can be found by consulting the phase plane (Figure 9b), where the conventional NES and the conventional with geometric damping are attracted to the slow left branch, and the BNES is attracted to the right branch even though the dynamics initiate well below the maximum of the SIM for the

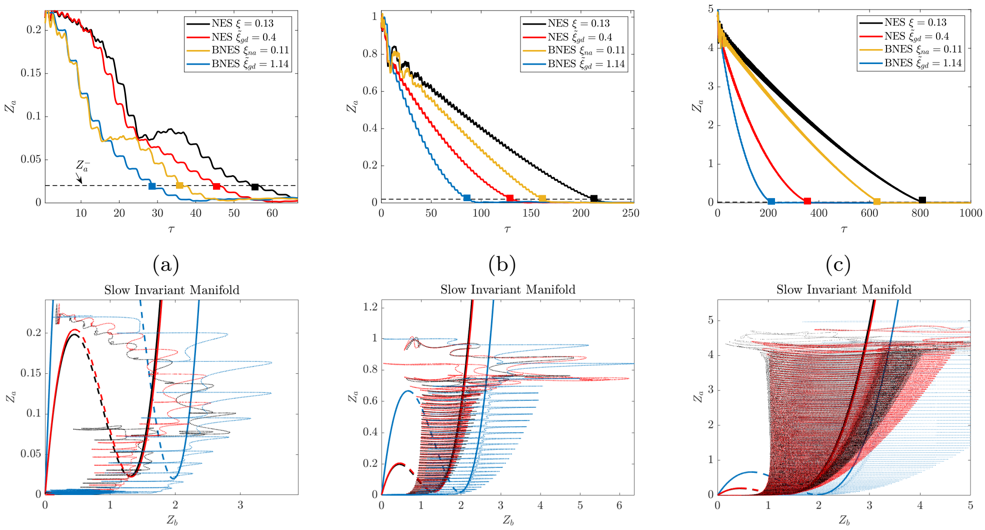

(a) (b) (c)

(d) (e) (f)

Figure 7: The envelope of the LO vibrations for $Z_a(0) = 0.202$ (a), $Z_a(0) = 1$ (b) and $Z_a(0) = 5$ (c), where the squares indicate when the residual energy is reached. On the phase plane of Z_a and Z_b the SIMs are compared to the simulation for $Z_a(0) = 0.202$ (d), $Z_a(0) = 1$ (e) and $Z_a(0) = 5$ (f). The BNES with linear damping (NES #3) is omitted from the bottom figures to not overload the figures. Black is NES #1, red NES #2, yellow NES #3 and blue NES #4.

BNES.

5. Numerical optimization of NESs

While the performance measures of the slow flow dynamics are fast to compute and may serve as qualitative performance measures. They are not accurate in measuring the absolute dissipation time. Therefore, a more accurate yet more computationally intensive hybrid scheme is proposed here that still uses numerical RK simulations while also incorporates some analytical aspects of the slow flow

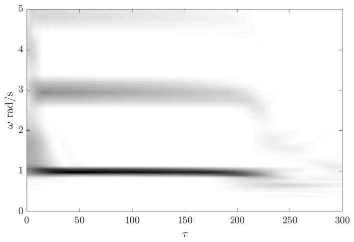

Figure 8: The wavelet transform of $\bar{z}$ of the NES #4 for $Z_a(0 = 5)$.

NES	T_{pump}	$T_{\text{pump,f}}$	$\Delta\%$
	$Z_a(0) = 0.202$		
NES #1	45.9	54.21	15
NES #2	38	44.8	15
NES #3	38.8	35.9	-5.8
NES #4	27	28.6	-5.9
	$Z_a(0) = 1$		
NES #1	195	213	8.5
NES #2	137	132	-3.8
NES #3	175	161	-8.7
NES #4	95	86.7	-9.6
	$Z_a(0) = 5$		
NES #1	771	809	4.7
NES #2	426	357	-19.3
NES #3	740	639	-15.8
NES #4	269	213	-26.3

Table 1: Comparison of pumping time and fast pumping time for three levels in initial energy. The parameters of the NES are mentioned at the beginning of Section 4.3. T_{pump} is computed with (31), $T_{\text{pump,f}}$ with (34) and $\Delta\%$ with (35).

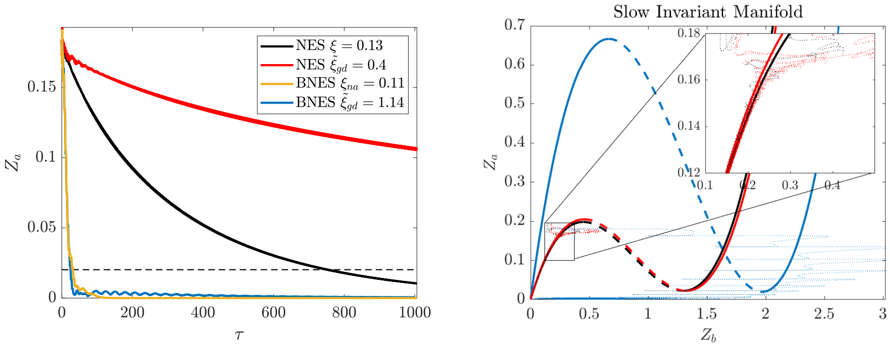

(a)

(b)

Figure 9: The envelopes (a) and phase plane (b) for $Z_a(0) = 0.18 < Z_a^+$ for the four NESs. The BNESs (NES#3 yellow, and NES #4 in blue) cause TET, even though the dynamics start below the maximum of the SIM.

dynamics. These measures will be computed from numerical simulation of the full EOM (33). Two performance measures are defined that will be obtained from the EOM that, similar to the slow flow measures, represents a measure for the *rate of dissipation* and a measure for the *residual energy.*

5.1. Performance measures

To quantify the rate of dissipation, the $y\%$ dissipation time is defined here as the time required for dissipating $y\%$ of the initial total energy $E_{\mathrm{tot}}(\tau)$ in the whole system:

$$T_{\mathrm{diss},y\%} = \{\tau : E_{\mathrm{tot}}(\tau) = (1 - y\%/100) \cdot E_{\mathrm{tot}}(0)\} \tag{36}$$

where the total energy is the sum of the kinetic and potential energy in the system:

$$E_{\mathrm{tot}}(\tau) = \frac{\bar{x}'^2(\tau)}{2} + \frac{\bar{x}^2(\tau)}{2} + \frac{\varepsilon(\bar{x}'(\tau) + \bar{z}(\tau)')^2}{2} + \frac{\kappa \bar{z}(\tau)^2}{2} + \frac{\bar{z}(\tau)^4}{4} \tag{37}$$

Here, the total energy is preferred over the energy in the LO, because the total energy is a monotonically decreasing function in time, while the energy only in the LO might go back and forth between the NES (beating). In the numerical simulations of the EOM, reaching $(1 - y\%/100)$ of the total energy is used as a stopping condition of the simulation. This decreases the computational effort significantly when investigating a vast space of coefficients. Here, the 70% dissipation time is studied, where the condition (36) is $\tau : E_{\mathrm{tot}}(\tau) = 0.3 \cdot E_{\mathrm{tot}}(0)$, a typically value [17]. To measure the degree of residual energy in the numerical simulations, the ratio of the $w\%$ dissipation time (or time with $(1-w)\%$ residual energy) and the y% dissipation time (or time with $(1 - y))\%$ residual energy) is computed, $w > y$. Here, it is opted for $w = 95\%$ and $y = 70\%$:

$$\tau_{\mathrm{res},5\%} = \frac{T_{\mathrm{diss},95\%}}{T_{\mathrm{diss},70\%}} \tag{38}$$

where a higher $\tau_{\mathrm{res},5\%}$ indicates that relative to the 70% dissipation time, it takes longer to dissipate to 95% of the total energy. As such, it is a relative measure of how long residual energy remains. The measure is referred to as the relative residual energy time.

5.2. Comparison of the four types of NESs

The 70% dissipation time and the relative residual energy time are determined for a conventional NES with linear damping ($\tilde{\xi}_{\mathrm{gd}} = 0$), a conventional NES with geometric damping $()\xi_{\mathrm{na}} = 0)$, a BNES with linear damping ($\tilde{\xi}_{\mathrm{gd}} = 0$ and $\kappa = 0.5$) and a BNES geometric damping ($\xi_{\mathrm{na}} = 0$, $\kappa = 0.5$ and $\tilde{f}^2(0) = 0.5$).

This is investigated for a range of damping values and initial energy $Z_a(0)$ where $\varepsilon = 0.02$ for all NESs. The results regarding the dissipation time are plotted in Figure 10 and the logarithm of the relative residual energy time in Figure 11. In both Figures, the conventional NES is Figure (a), the conventional NES with geometric damping is Figure (b), the BNES with linear damping is Figure (c) the BNES with geometric damping is Figure (d) .

Considering the dissipation time, Figure 10, all NES have an optimal zone where the dissipation time is the lowest (dark blue zone). The threshold value Z_a^+, computed from (26) is plotted on the Figures for the conventional NES as the full white line, Figures 10a and 10b. For $\xi_{na} > 1/\sqrt{3}$, the SIM for the NES with linear damping has no maximum. This line approximately separates the parameter space between an efficient (blue) and an inefficient (red) zone. For the conventional NES, the maximum of the SIM is thus a valid energy threshold over a wide range. Regarding the BNESs, Figures 10c and 10d, it is the minimum of the SIM, Z_a^-, that predicts well the zones of efficient and inefficient BNES. To the left of this line, the BNESs performance is worse but not as bad as the conventional NES. This is because of chaotic vibrations [18, 37, 38]. Compared to the BNES with nonlinear damping, the BNES with linear damping has a larger area to the left of this line, where the performance is reduced. To the left of the grey full line in Figure 10c, the BNES with linear damping also has a very low dissipation time. This is when the BNES stays near one of its stable points, acting as a linear tuned mass damper [17, 18]. Unlike the white full line, this grey full line is not computed analytically but drawn on the Figure to mark an efficient area. In absolute terms, the BNES with nonlinear geometric damping is the best-performing NES, with lower dissipation times over larger zones in the parameter space. The conventional NES with geometric damping performs better than the conventional NES but has the worst performance to the left of the threshold line. Finally, the BNES with linear damping is the best type of NES in the lower energy regions.

All dissipation time figures also have a dotted grey line. These stem from the relative residual energy time plots, which is explained next.

Regarding the residual energy measure, all NESs have a low residual energy zone (dark blue) and a high residual energy zone (light blue to red), separated on Figure 11 by the dotted grey line. This line is drawn from observation, not from an analytical formula. It is this dotted line that is also plotted on the dissipation time plots, Figure 10. When the logarithm of the relative residual energy time near 0 (dark blue) means that the dissipation times for 70% and 95% are close. The delimitation of the high and low residual energy zones mainly depends on the damping. So, although some high damping values may have brought a low dissipation time in Figure 10, it may correspond to a high residual energy.

The design an NES, the designer should focus on the optimal areas in Figure 10 to the right of the full white line and, if residual energy is not desired, below the grey dotted line. The threshold value is computed analytically, while numerically, the best absolute dissipation time is computed.

5.3. *Influence of κ on the BNES performance*

While the performance for the conventional NES and NES with geometric damping can be assessed in the ξ_{na}-$Z_a(0)$ parameter space, the BNES has an additional parameter, the negative linear stiffness κ. The dissipation time for $\kappa = 0.25$, $\kappa = 0.5$ and $\kappa = 0.75$ are plotted on Figure 12. The threshold between TET and chaotic vibrations shifts to the right as κ increases. Additionally, the zones of lowest dissipation time shift to lower $\tilde{\xi}_{\mathrm{gd}}$ values as κ increases.

5.4. *Optimization of the BNES for robust vibration control*

Although the above-discussed performance plots allow tuning a well-performing NES, these show that the zone of lowest dissipation speed is just to the right of a threshold lines. A slight decrease in initial energy $Z_a(0)$ because of uncertainty or change of operation in the LO will yield a high dissipation time. Therefore, an optimization scheme is proposed to obtain a robust BNES with geometric damping. The goal is to tune a BNES that is robust for a range of initial energies. To take robustness around a central $Z_a(0)$ in consideration, the following cost function is proposed:

$$J(\kappa, \tilde{\xi}_{\mathrm{gd}}) = \frac{1}{3} T_{\mathrm{diss,70\%}}(0.5 Z_a(0)) + \frac{1}{3} T_{\mathrm{diss,70\%}}(Z_a(0)) + \frac{1}{3} T_{\mathrm{diss,70\%}}(2 Z_a(0)) \quad (39)$$

This cost function will also take into account (with equal weights) the dissipation time for half and double the initial energy to ensure a fast dissipation for the whole range of $[0.5Z_a(0), 2Z_a(0)]$. Other ranges can, of course also be proposed. The logarithm of the cost function for $Z_a(0) = 1$ in function of κ and $\tilde{\xi}_{\mathrm{gd}}$ is shown in Figure 13. A narrow zone in the $\tilde{\xi}_{\mathrm{gd}} - \kappa$ parameter space delimitates a robust BNES. For higher κ a lower damping coefficient $\tilde{\xi}_{\mathrm{gd}}$ is optimal. The most optimal point, indicated by the grey square, is where $\kappa = 1.04$ and $\tilde{\xi}_{\mathrm{gd}} = 1.16$

6. Harmonic excitations

6.1. *Equations of motion and Harmonic balancing*

The NES performance is now investigated for the harmonically excited LO. A force with frequency ω and magnitude F is added to equation (11):

$$\begin{aligned} &m\ddot{x} + c\dot{x} + kx + c_{\mathrm{na}}(\dot{x} - \dot{x}_{\mathrm{na}}) + c_{\mathrm{gd}}(x - x_{\mathrm{na}})(\dot{x} - \dot{x}_{\mathrm{na}}) + F_{\mathrm{s}}(x - x_{\mathrm{na}}) = F\cos(\omega t) \\ &m_{\mathrm{na}}\ddot{x}_{\mathrm{na}} - c_{\mathrm{na}}(\dot{x} - \dot{x}_{\mathrm{na}}) - c_{\mathrm{gd}}(x - x_{\mathrm{na}})(\dot{x} - \dot{x}_{\mathrm{na}}) - F_{\mathrm{s}}(x - x_{\mathrm{na}}) = 0 \end{aligned} \quad (40)$$

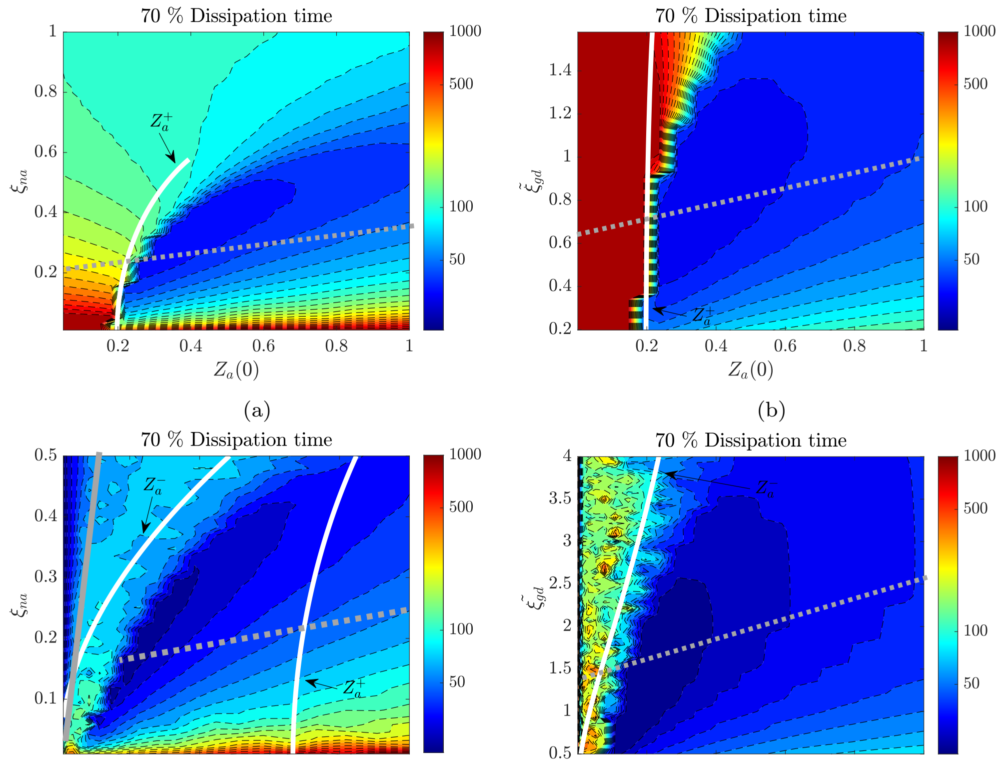

(a) (b)

(c) (d)

Figure 10: Dissipation time for conventional NES (a), NES with geometric damping (b), BNES with linear damping ($\kappa = 0.5$) (c)and BNES with geometric damping ($\kappa = 0.5$ and $\tilde{f}^2(0) = 0.5$) (d) . For each configuration $\xi = 0$. White full lines are analytically computed threshold values (Z_a^+ for the NESs and Z_a^- for the BNESs). The grey dotted lines separates the parameters space in low and high relative residual energy time, obtained from Figure 11. The grey full line in (c) separates chaotic and interwell vibrations.

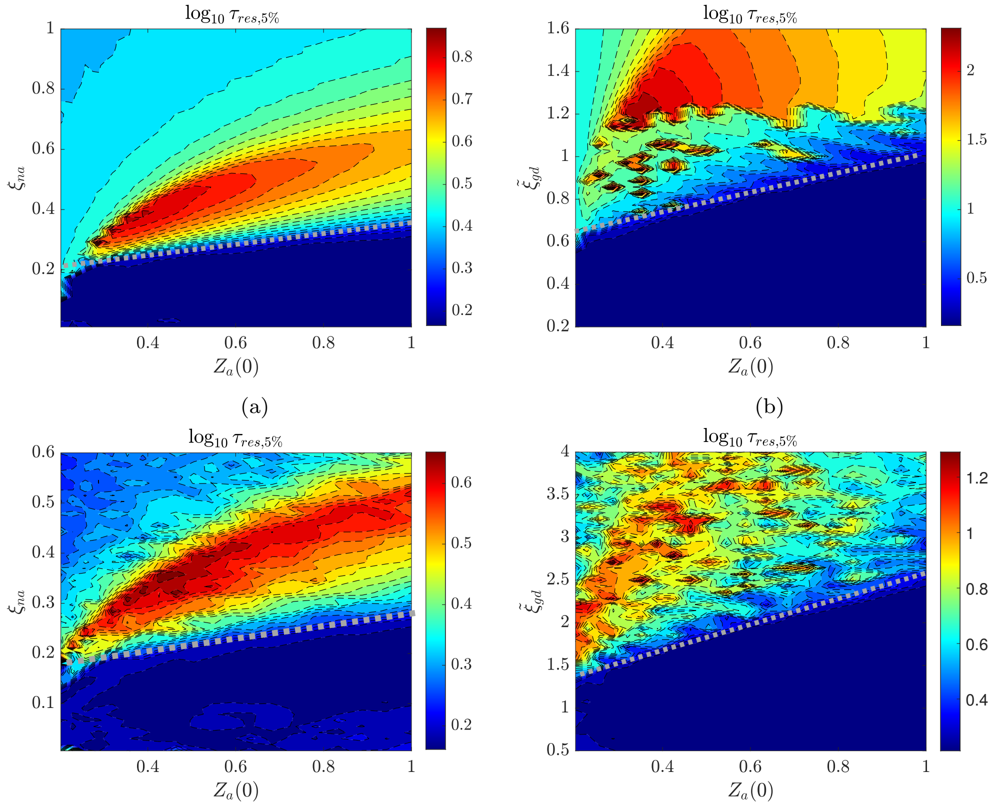

(a)

(b)

(c)

(d)

Figure 11: Residual energy for conventional NES (a), NES with geometric damping (b), BNES with linear damping (c) and BNES with geometric damping (d).

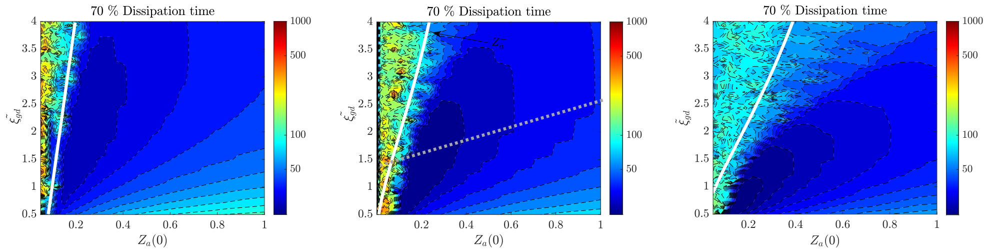

(a)

(b)

(c)

Figure 12: Dissipation time for BNES with geometric damping with $\kappa = 0.25$ (a), $\kappa = 0.5$ (b) and $\kappa = 0.75$ (c).

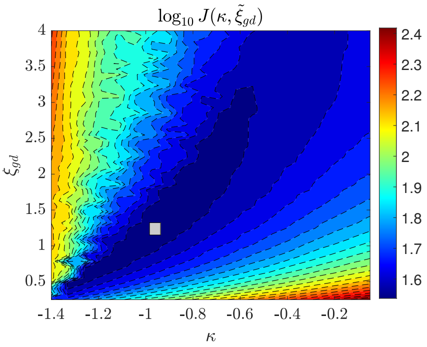

Figure 13: Tuning a robust BNES with geometric damping where $\tilde{f}^2(0) = 0.5$. Cost function (39) is computed logarithmically. The grey square signifies the minimum of the cost function.

In dimensionless time, $\tau = \omega_n t$, and relative absorber coordinate ($z = x_{\mathrm{na}} - x$) the EOM become:

$$\begin{aligned} x'' + \varepsilon \xi x' + x + \varepsilon \left(z'' + x'' \right) &= \varepsilon P \cos(\Omega \tau) \\ \varepsilon \left(z'' + x'' \right) + \varepsilon \xi_{na} z' + \varepsilon \xi_{\mathrm{gd}}(z) z' + \varepsilon f_{\mathrm{s}}(z) &= 0 \end{aligned} \tag{41}$$

where $P = \frac{F}{\omega_n^2 m_{\mathrm{na}}}$ and $\Omega = \frac{\omega}{\omega_n}$.

As in the transient case, only the NES and BNES with (geometric) damping will be studied, with the stiffness and damping forces reported in (14) and (16). Then, with dimensionless displacement $\bar{x} = \sqrt{\gamma} x$ and $\bar{z} = \sqrt{\gamma} z$, (41) becomes:

$$\begin{aligned} &\bar{x}'' + \varepsilon \xi \bar{x}' + \bar{x} + \varepsilon \left(\bar{z}'' + \bar{x}'' \right) = \varepsilon \bar{P} \cos(\Omega \tau) \\ &\varepsilon \left(\bar{z}'' + \bar{x}'' \right) + \varepsilon \xi_{na} \bar{z}' + \varepsilon \frac{\tilde{\xi}_{\mathrm{gd}}}{4} \bar{z}^2 \bar{z}' \frac{\left(\bar{z}^2 - \kappa \right)^2}{\frac{\bar{z}^4}{4} - \frac{\kappa}{2} \bar{z}^2 + \tilde{f}(0)^2} + \bar{z}^3 - \kappa \bar{z} = 0 \end{aligned} \tag{42}$$

where $\bar{P} = P\sqrt{\gamma}$. The next step is HB in a single frequency Ω. The following complex Manevitch variables facilitate this:

$$2A(\tau) e^{i\tau} = \bar{x} - i \frac{\bar{x}'}{\Omega} \quad 2B(\tau) e^{i\tau} = \bar{z} - i \frac{\bar{z}'{}'}{\Omega} \tag{43}$$

where the original variables are then substituted by:

$$\begin{aligned} \bar{x} &= A(\tau) e^{i\Omega\tau} + A^*(\tau) e^{-i\Omega\tau} & \bar{z} &= B(\tau) e^{i\Omega\tau} + B^*(\tau) e^{-i\Omega\tau} \\ \bar{x}' &= i\Omega (A(\tau) e^{i\Omega\tau} - A^*(\tau) e^{-i\Omega\tau}) & \bar{z}' &= i\Omega (B(\tau) e^{i\Omega\tau} - iB^*(\tau) e^{-i\Omega\tau}) \\ \bar{x}'' + \Omega \bar{x} &= i2\Omega \dot{A} e^{i\Omega\tau} & \bar{z}'' + \Omega \bar{z} &= i2\Omega \dot{B} e^{i\Omega\tau} \end{aligned} \tag{44}$$

Substituting (44) into (42) and keeping only the terms with frequency Ω yields:

$$\begin{aligned} &i2\Omega\dot{A} + i\varepsilon\zeta\Omega A + (1-\Omega^2)A + \varepsilon(i2\Omega\dot{B} - \Omega^2 B + i2\Omega\dot{A} - \Omega^2 A) = \frac{\varepsilon\bar{P}}{2} \\ &i2\Omega\dot{B} + 2i\Omega\dot{A} - \Omega^2 B - \Omega^2 A + \xi_{\text{na}} i\Omega B + \tilde{\xi}_{\text{gd}} i\Omega B\tilde{H}(|B|) + BG(|B|) = 0 \end{aligned} \tag{45}$$

where H and G are the same expressions as for the transient case. In steady state ($\dot{A} = \dot{B} = 0$), (45) is reduced to:

$$\begin{aligned} i\zeta\sqrt{X}A + \sigma A - XB - XA &= \frac{\bar{P}}{2} \\ -XB - XA + \xi_{\text{na}} i\sqrt{X}B + \tilde{\xi}_{\text{gd}} i\sqrt{X}B\tilde{H}(B, B^*) + BG(B, B^*) &= 0 \end{aligned} \tag{46}$$

with $X = \Omega^2$ and $\varepsilon\sigma = 1 - X$. The stability of the steady state solutions is computed in Appendix C. Next, the equations can be manipulated to obtain two equations in $Z_a = a^2$ and $Z_b = b^2$ with $A = \frac{a}{2}e^{i\alpha}$ and $A = \frac{b}{2}e^{i\beta}$. The first one is a SIM between Z_a and Z_b:

$$X^2 Z_a = Z_b\left(X\left(\xi_{\text{na}} + \tilde{\xi}_{\text{gd}}\tilde{H}(Z_b)\right)^2 + (X - G(Z_b))^2\right) \tag{47}$$

and the second a SIM that relates Z_b with $\bar{P}$:

$$\begin{aligned} &\left[(X-\sigma)(G(Z_b) - X) + X\xi_{\text{na}}\xi + X\tilde{\xi}_{gd}\xi\tilde{H}(Z_b) + X^2\right]^2 Z_b \\ &+ X\left[\xi(G(Z_b) - X) + (\sigma - X)(\xi_{\text{na}} + \tilde{\xi}_{\text{gd}}\tilde{H}(Z_b))\right]^2 Z_b \\ &= \left(X\bar{P}\right)^2 \end{aligned} \tag{48}$$

Per excitation level $\bar{P}$, a frequency response can be computed by first solving (48) for Z_b and computing the corresponding Z_a from (47). The frequency responses obtained from HB (referred to as HB FR) are now compared to time simulations from the full EOM, (42). The same NESs #1-#4 as mentioned in the beginning of Section 4.3 are studied. This time, the LO has a damping ratio of $\xi = 0.5$, which corresponds with a damping ratio of 0.5%.

6.2. Comparison Runga-Kutta and Harmonic Balancing: conventional NESs (NES #1 and #2)

6.2.1. Characteristic regimes

The relation between the HB FR and the RK simulation for NES #1 (the conventional NES with linear damping) is studied in detail in Figure 14. Figure 14a shows the HB FR for several levels of $\bar{P}$, where $a = \sqrt{Z_a}$, and Figure 14b features two SIMs computed from (47) for $\Omega = 1$ and $\Omega = 0.965$. The full lines correspond to stable solutions, while the dashed correspond to unstable solutions. These SIMs have the distinctive S-shape similar to the transient case. The amplitude a corresponding with the maximum and minimum of the SIM, $\sqrt{Z_a^+}$ and $\sqrt{Z_a^-}$, are drawn as the black dashed line on Figure 14a.

Similar to the transient case, the maximum and minimum of the SIM play an important role in explaining the behavior of the NES near resonance. As the load magnitude increases, the HB FR (Figure 14a) distorts and saturates around the Z_a^+ line, where the response is unstable. For $P = 0.7$, a bifurcation creates an isolated response between $\Omega = 0.96$ and 0.98. This isola is an undesirable response, as it has a much higher a amplitude than without the NES.

The RK simulations are done for $\bar{P} = 0.7$ at resonance $\Omega = 1$ and at $\Omega = 0.965$, as noted in yellows squared on the FR. The latter frequency has the isola solutions, and is simulated for $x'(0) = 0$ and $x'(0) = 0.5$. The time simulations are presented in Figures 14c to 14e, and in state space on the SIM of Figure 14b. For $\Omega = 1$, Figure 14c, the so-called strongly modular response (SMR) occurs, where the vibrations of both the NES and the LO modulate. The blue color on the time simulations indicates the envelope, which is also plotted in state space. The mechanism behind the SMR is the SIM. Just like for the transient case, the right branch of the SIM is descended, where the LO vibration's amplitude decreases. Once the minimum of the SIM is reached, the dynamics go to the left branch. Unlike the transient case however, the dynamics now climb up the left branch. Once the maximum of the SIM is reached, the dynamics return to the right branch. This explains the periodic modulation of the vibration amplitude. The minimum and maximum of the SIM, $\sqrt{Z_a^+}$ and $\sqrt{Z_a^-}$, indicate this modulation's maximum and minimum amplitude. The SMR occurs for frequencies around resonance where the branch is unstable [10].

For $\Omega = 0.965$, the HB FR has three solutions. The RK simulation for $x'(0) = 0$, Figure 14d has a low amplitudes and is on the left branch on the SIM, and on the main branch of the HB FR. For $x'(0) = 0.5$, Figure 14e, both the LO and NES have a higher amplitude, indicating it is on the isola on the HB FR. This shows that the isola are detrimental for the NES vibration control performance. NES #2 has nonlinear damping but has the same characteristic regimes, so the analysis is not repeated.

6.2.2. Comparing NES #1 and NES #2

The HB FR and RK conventional NES with linear and nonlinear damping are now compared with for $\bar{P} = 0.9$ in Figure 15. The HB FR is shown in black,

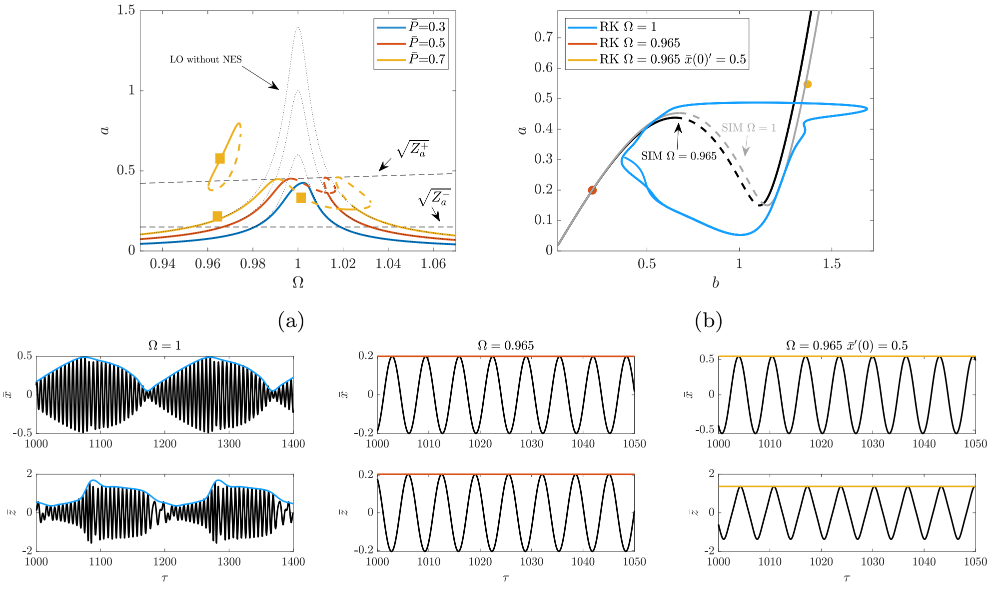

(a)

(b)

(c)

(d)

(e)

Figure 14: Comparing HB and RK and characteristic regimes for NES #1 ($\xi_{\text{na}} = 0.13$ and $\tilde{\xi}_{\text{gd}} = \kappa = 0$) . FR from HB (a) for several levels of $\bar{P}$ (a) with stable (full) and unstable (dashed) responses, SIMs for two different frequencies (b), RK for $\Omega = 1$ (c), RK for $\Omega = 0.965$ and $\bar{x}'(0) = 0$ (d) and $\bar{x}'(0) = 0.5$. (e)

the maximum and minimum of the SIM in black dashed and the RMS value of the RK simulation as blue dots. When there is SMR, the vibrations modulate. To indicate this on the FR, the RK's minimum and maximum amplitude are also plotted with the orange and yellow dots, respectively. Figure 15a is the FR for NES #1 and Figure 15b for NES #2. For both NESs, the RK RMS follows the HB curve, until the HB curve saturates around the $\sqrt{Z_a^+}$-line. At that point, the RK shows SMR, with RMS max approximately equal to $\sqrt{Z_a^+}$ and RMS min approximately equal to $\sqrt{Z_a^-}$. However, The HB FR value does not represent the RK RMS value. Observing the HB, the isola for NES #1 is much larger. Furthermore, between $\Omega = 0.97$ and $\Omega = 0.98$, the RK RMS is on the isolated response, even though each simulation has $x'(0) = 0$. Although NES #2 also has an isola, the RK RMS is never on it and the isola corresponds to lower a. Furthermore, at resonance $\Omega = 1$, the RMS of NES #1 is 0.36 while NES #2 is 0.29. The geometric nonlinear damping has a lower RMS response and is more robust against the high responses of the isolas.

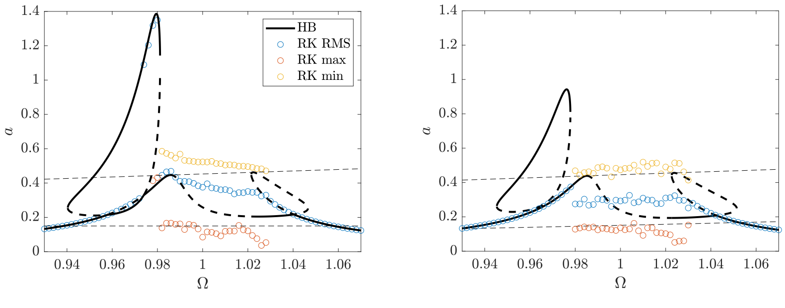

(a)

(b)

Figure 15: Frequency response from HB (black) and RK (dots) around resonance, (a) for NES #1 ($\xi_{\text{na}} = 0.13$ and $\tilde{\xi}_{\text{gd}} = \kappa = 0$) and (b) NES #2 ($\tilde{\xi}_{\text{gd}} = 0.4$ and $\xi_{\text{na}} = \kappa = 0$).

6.3. Comparison Runga-Kutta and Harmonic Balancing: Bistable Stiffness

6.3.1. Characteristic regimes

Figure 16 investigates the relation between HB and RK in the case of NES # 3, the bistable NES with linear damping. Figure 16a shows the FR from HB. Compared to the FR of NES #1, Figure 14a, the $\sqrt{Z_a^+}$ is much higher is much higher. For $\Omega = 1$, the time simulation and phase plane are shown in Figure 16c and 16b, respectively. Although this is SMR, the phase plane shows that the maximum of the SIM is not reached. The right branch is descended, however, once the minimum of the SIM is reached, the NES vibrates chaotically in the time simulation. Then, the dynamics again go to the right branch, to descend the SIM again. This process repeats. The energy threshold, the vibration amplitude in the LO for which the NES activates, is much lower than the maximum of the SIM, just like in the transient case for BNESs

Other vibration regimes are the interwell vibrations at $\Omega = 0.93$, Figure 16d, and purely chaotic vibrations, Figure 16e. As the HB scheme does not model these regimes, these vibration regimes are not situated on the SIM, Figure 16b. Furthermore, these regimes don't result in significant vibration damping [37, 38].

6.3.2. Comparing NES #3 and NES #4

To better understand the vibration damping performance for bistable NESs, the HB FR is now compared to RK simulations for $\bar{P} = 0.9$ for NES #3 on Figure 17a and for NES # 4 on Figure 17b. Both NES have similar behavior. The RK RMS follows the HB FR until the minimum and maximum values diverge under SMR. From that point, the RK min follows the $\sqrt{Z_a^-}$ line closely, the minimum of the SIM, while the RK max is much lower than the $\sqrt{Z_a^+}$ line. This is because under the SMR regime, the dynamics do not fully climb the SIM. The RMS is,

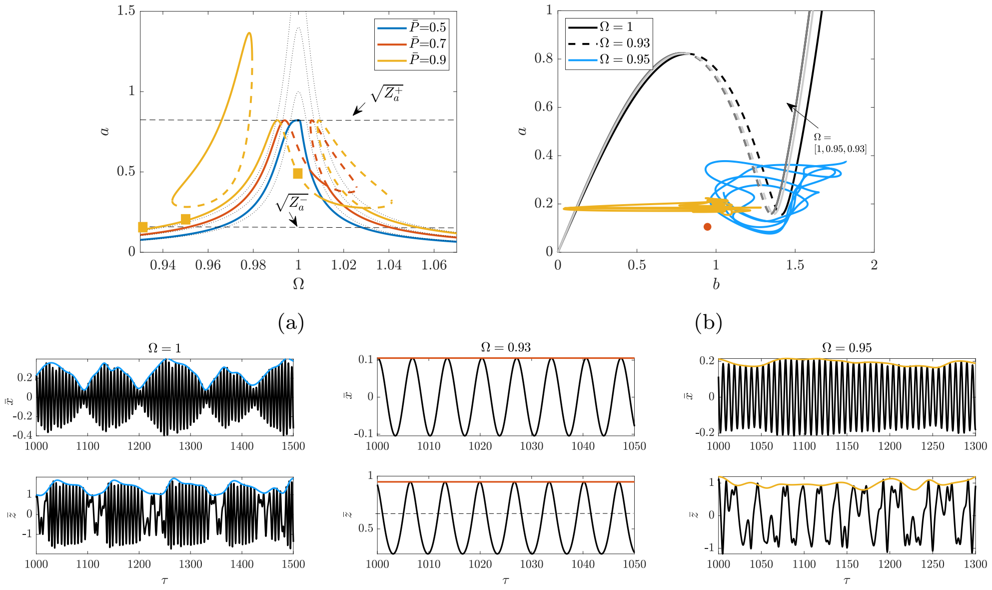

(a) (b)

(c) (d) (e)

Figure 16: Comparing HB and RK and characteristic regimes, for NES #3 ($\xi_{\text{na}} = 0.11$, $\tilde{\xi}_{\text{gd}} = 0$ and $\kappa = 0.5$). FR from HB (a) for several levels of $\bar{P}$ with stable (full) and unstable (dashed) responses, SIMs for two different frequencies (b), RK for $\Omega = 1$ (c), RK for $\Omega = 0.93$ (d) and $\Omega = 0.95$ (e).

for the most part, under the HB line. As such, near resonance, the HB FR value is not representative for the RMS and maximum value of the RK. The RK min is predicted well by the $\sqrt{Z_a^-}$ line. The main difference between the two NESs is the much smaller isola for NES #4, thus confirming that nonlinear damping has a positive effect in reducing the isola. The RMS of NES #3 is 0.28 while NES #4 is 0.24.

7. Parameter study and Isola tuning

7.1. Effect of isola

When comparing the HB FR and RK under SMR, the HB FR can predict the maximum and minimum of the modulation for NESs # 1 and #2, but only the minimum of the modulation for bistable NESs, NES# 3 and #4. Furthermore, the amplitude obtained from HB does not represent the RK RMS under SMR.

The HB FR also indicates when an isola appears, and when the isola touches the main branch. In Figure 15a, the isola touches the main branch, and for some

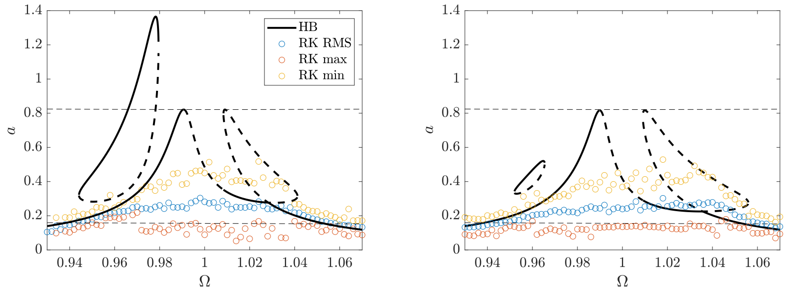

(a) (b)

Figure 17: Frequency response from HB and RK around resonance, (a) for NES #3, ($\xi_{\text{na}} = 0.11$, $\tilde{\xi}_{\text{gd}} = 0$ and $\kappa = 0.5$) and (b) NES #4 ($\xi_{\text{na}} = 0$, $\tilde{\xi}_{\text{gd}} = 1.14$, $\kappa = 0.5$ and $\tilde{f}^2(0) = 0.5$.)(b).

Ω, the response goes to the top stable branch, resulting in undesirable high amplitude vibrations. For zero initial conditions, the RK simulation will only go to the isola if the isola touches the main branch. This conjecture is tested in Figure 18a. For a conventional NES with linear damping, the $\bar{P}$ for which the isola appears and touches is computed from HB, in function of ξ_{na}. For $\xi_{na} = 0.13$ (=NES #1) the isola appears for $\bar{P} = 0.67$ and touches the main branch at $\bar{P} = 0.88$. Then, with RK simulations with zero initial conditions, the value for $\bar{P}$ where the RK RMS jumps to the isola is detected. Figure 18a confirms numerically that jumping to a higher branch will happen in the RK simulation if the isola touches the main branch.

A hybrid approach incorporating HB and RK is proposed to design the NES. The vibration amplitude of the LO at resonance (Ω=1) is obtained from RK simulations rather than HB, as the HB FR does not accurately represent the vibration amplitude at SMR. The HB FR will be used to find when the isola appears and touches the main branch. A designer can then opt to tune such that the isola does not touch the branch or that no branch appears at all. The latter is safer if initial conditions may occur that put the dynamics in the isola, even if the isola does not touch the main branch.

7.2. Parameter study

Figures 19 and 20 plot the RK RMS values at resonance of the LO with the conventional NES with (non)linear damping and BNES with (non)linear damping, respectively. The load range is $\bar{P} = [0, 2]$ while the damping ranges are chosen such that an RMS value of 1.2 is the maximum value.

For each configuration, the lines where isolas appear (white dotted) and isolas touch the main branch (white dash) are plotted. Below the isola lines, there are mainly vertical contour lines, which implies that for a given damping, the RMS

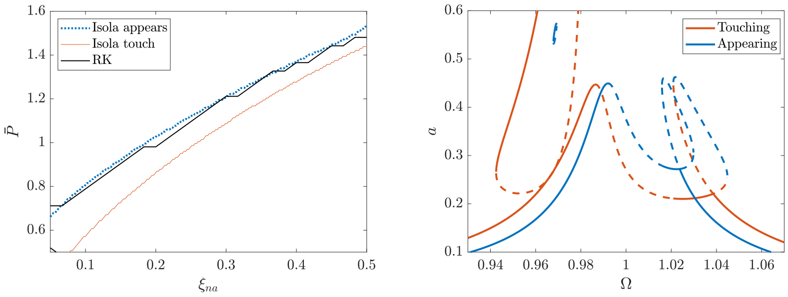

(a) (b)

Figure 18: (a) The $\bar{P}$ where isola appears (red dash) and touches the main branch (blue dotted) for HB and when the upper stable isola branched in reached in RK (black), for a range of ξ_{na}. (b) For $\xi_{\text{na}} = 0.13$, the isola appears for $\bar{P} = 0.67$ and touches the FR for $\bar{P} = 0.88$. $\kappa = \tilde{\xi}_{\text{gd}} = 0$.

value saturates over a range of $\bar{P}$. Above the isola lines the contour lines become more horizontal, indicating increasing RMS with increasing force magnitude $\bar{P}$. When comparing the RMS of the conventional NES and BNES with linear damping (Figures 19a and 20a) to those with nonlinear damping (Figures19b and 20bà, the NESs with nonlinear damping have a larger area with lower RMS values than the NESs with linear damping. Especially, the BNES with nonlinear damping has the most blue, ’optimal’, regions.

To design an NES, it opted here to tune the damping such that for a particular $\bar{P}_{\text{tune}}$, the isola touches the main branch. As such, the NES is robust for excitations until this tuned load magnitude. The RMS value at resonance may still be low above $\bar{P}_{\text{tune}}$, as the isola are to to the left of resonance. The the jump to the isola will only occur under slight shifts of the forcing frequency or on ramp up or ramp down. The tuning can be done visually on the Figures 19 and 20 by drawing a horizontal line at $\bar{P}_{\text{tune}}$ and finding the corresponding value where this line intersects the white dashed isola touching the line.

For $\bar{P}_{\text{tune}} = 1$, this obtains a conventional NESs with linear damping $\xi_{\text{na}} = 0.19$ and nonlinear damping $\tilde{\xi}_{\text{gd}} = 0.46$ and BNESs with linear damping $\xi_{\text{na}} = 0.14$ and nonlinear damping $\tilde{\xi}_{\text{gd}} = 0.7$. For this tuning, the RK RMS at resonance for a range of $\bar{P}$ is shown in Figure 21a. Despite increasing load magnitude, all NESs have a range where the RMS saturates. Beyond $\bar{P} = 1$, where the isola touches the main branch, the saturation is lost and the RMS increases after a sharp decrease. If further robustness is required, $\bar{P}_{\text{tune}}$ can be increased to 1.5. Figure 21b shows the obtained damping values and RMS. Similarly, a saturation region is seen, followed by a loss of saturation. For each tuning, the NESs with nonlinear damping perform better than their linear damping counterparts. For $\bar{P} = 1$, the BNES with linear damping performs similarly to the conventional NES with nonlinear damping. However, for $\bar{P} = 1.5$, both NESs with nonlinear

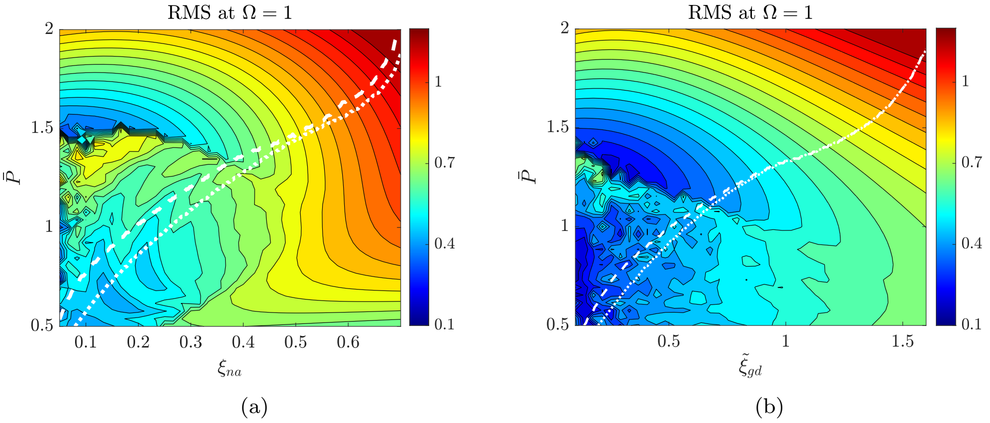

Figure 19: The RK RMS at $\Omega = 1$ in function of ξ_{na} and $\bar{P}$ for conventional NES with linear damping (a), $\kappa = \tilde{\xi}_{\text{gd}} = 0$, and function of $\tilde{\xi}_{\text{gd}}$ and $\bar{P}$ for conventional NES with nonlinear geometric damping, (b) $\kappa = \xi_{\text{na}} = 0$. The dotted white line is when the isola appears in the HB FR, and the white dashed line when the isola touches the main branch.

damping are much better than the NESs with linear damping. For both $\bar{P}_{\text{tune}}$s, the BNES with nonlinear damping is the superior NES.

8. Conclusion

In this paper, a device was proposed to tailor nonlinear stiffness and nonlinear geometric damping. It consists of a mass-spring-damper where the ends of a linear spring and a linear damper are compressed according to some function that generates a nonlinear damping and spring force. The methodology allows tailor-making of both nonlinear spring and damping forces. This device is used here to obtain an NES that damps vibrations for a main structure that is a linear oscillator. In particular, the nonlinear geometric damping obtained from hardening and bistable stiffness (the BNES) are studied. Harmonic balancing was applied and a slow invariant manifold (SIM) was obtained for impulsive loading. From the SIM, two performance measures were derived, the residual energy and the pumping time for generic nonlinear spring force and nonlinear damping. These measures showed was found that the bistable NES with nonlinear damping is the most efficient and robust NES. However, for high impulsive loads, these performance measures were not accurate in the describing the actual performance of the full equations of motion (EOM), because of the existence of higher harmonics. Therefore, a dissipation time and residual energy measure were defined for numerical simulations of the full EOM, which describe NES performance more accurately. These measures also showed that the BNES with nonlinear damping is the more

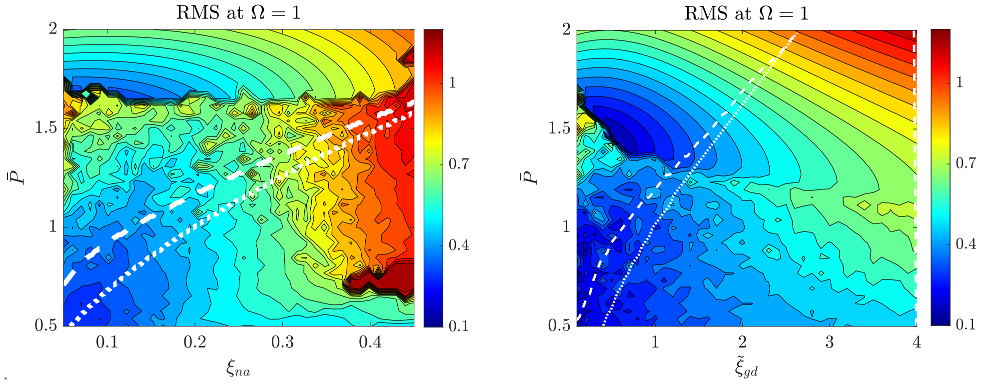

(a) (b)

Figure 20: The RK RMS at $\Omega = 1$ in function of ξ_{na} and $\bar{P}$ for bistable NES with linear damping (a), $\kappa = 0.5$, $\tilde{\xi}_{\text{gd}} = 0$, and function of $\tilde{\xi}_{\text{gd}}$ and $\bar{P}$ for bistable NES with nonlinear geometric damping (b), $\kappa = 0.5$, $\xi_{\text{na}} = 0$ and $\tilde{f}^2(0) = 0.5$. The dotted white line is when the isola appears in the HB FR, and the white dashed line when the isola touches the main branch.

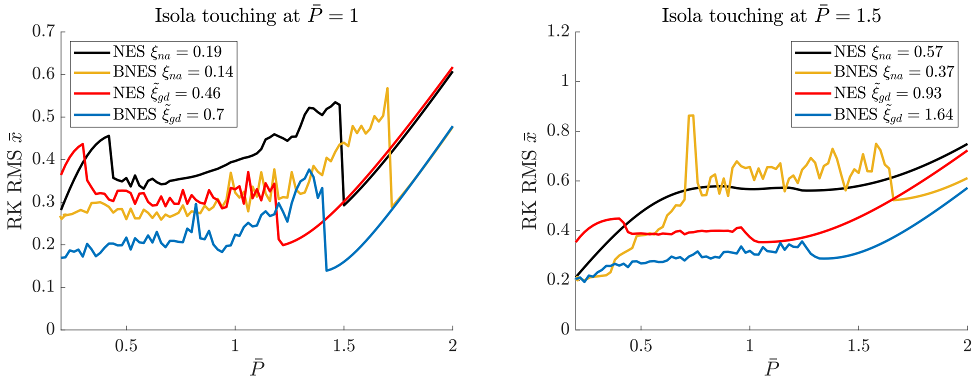

(a) (b)

Figure 21: Tuning to avoid isola touching at $\bar{P}_{\text{tune}} = 1$ (a) and $\bar{P}_{\text{tune}} = 1.5$ (b) for NES with linear and nonlinear damping, and BNES ($\kappa = 0.5$) with linear and nonlinear damping ($\tilde{f}^2(0) = 0.5$) .

robust and efficient NES of the investigated configurations. A hybrid approach to tune the NES was proposed, using both the analytical tools from the SIM and the numerical measures. The NES performance under harmonically loaded linear oscillator was also investigated. Under the strongly modulated response regime, the LO's vibrations are reduced greatly around resonance. However, the frequency response obtained from harmonic balancing showed isolated responses, with high LO amplitudes. A tuning scheme was proposed based on the existence of this isola. The NESs with nonlinear damping, especially the BNES, were shown to be the best NES configuration under this scheme. The proposed device opens up a whole new area of study of nonlinear damping types that, up until now, were typically only limited to $z^2\dot{z}$ because of existing devices so far. Future research will focus on the realization of the proposed device, and optimization of the device's shape to obtain other stiffness than bistable or hardening.

References

[1] J. P. Den Hartog, Mechanical vibrations, Courier Corporation, 1985.

[2] C.-L. Lee, Y.-T. Chen, L.-L. Chung, Y.-P. Wang, Optimal design theories and applications of tuned mass dampers, Engineering structures 28 (1) (2006) 43–53.

[3] L. Zuo, S. A. Nayfeh, Optimization of the individual stiffness and damping parameters in multiple-tuned-mass-damper systems, J. Vib. Acoust. 127 (1) (2005) 77–83.

[4] A. F. Vakakis, O. V. Gendelman, L. A. Bergman, D. M. McFarland, G. Kerschen, Y. S. Lee, Nonlinear targeted energy transfer in mechanical and structural systems, Vol. 156, Springer Science & Business Media, 2008.

[5] H. Ding, L.-Q. Chen, Designs, analysis, and applications of nonlinear energy sinks, Nonlinear Dynamics 100 (4) (2020) 3061–3107.

[6] A. F. Vakakis, O. V. Gendelman, L. A. Bergman, A. Mojahed, M. Gzal, Nonlinear targeted energy transfer: state of the art and new perspectives, Nonlinear Dynamics 108 (2) (2022) 711–741.

[7] K. Dekemele, R. De Keyser, M. Loccufier, Performance measures for targeted energy transfer and resonance capture cascading in nonlinear energy sinks, Nonlinear Dynamics 93 (2018) 259–284.

[8] G. Habib, F. Romeo, Tracking modal interactions in nonlinear energy sink dynamics via high-dimensional invariant manifold, Nonlinear Dynamics 103 (4) (2021) 3187–3208.

[9] O. Gendelman, Y. Starosvetsky, M. Feldman, Attractors of harmonically forced linear oscillator with attached nonlinear energy sink i: description of response regimes, Nonlinear Dynamics 51 (2008) 31–46.

[10] B. Vaurigaud, A. Ture Savadkoohi, C.-H. Lamarque, Targeted energy transfer with parallel nonlinear energy sinks. part i: Design theory and numerical results, Nonlinear dynamics 66 (2011) 763–780.

[11] Y.-c. Zeng, H. Ding, A tristable nonlinear energy sink, International Journal of Mechanical Sciences 238 (2023) 107839.

[12] B. Bergeot, Effect of stochastic forcing on the dynamic behavior of a self-sustained oscillator coupled to a non-linear energy sink, International Journal of Non-Linear Mechanics (2023) 104351.

[13] J. Wang, B. Wang, N. E. Wierschem, B. F. Spencer Jr, Dynamic analysis of track nonlinear energy sinks subjected to simple and stochastice excitations, Earthquake Engineering & Structural Dynamics 49 (9) (2020) 863–883.

[14] O. V. Gendelman, C. Lamarque, Dynamics of linear oscillator coupled to strongly nonlinear attachment with multiple states of equilibrium, Chaos, Solitons & Fractals 24 (2) (2005) 501–509.

[15] F. Romeo, L. Manevitch, L. Bergman, A. Vakakis, Transient and chaotic low-energy transfers in a system with bistable nonlinearity, Chaos: An Interdisciplinary Journal of Nonlinear Science 25 (5) (2015) 053109.

[16] M. A. Al-Shudeifat, A. S. Saeed, Frequency–energy plot and targeted energy transfer analysis of coupled bistable nonlinear energy sink with linear oscillator, Nonlinear Dynamics 105 (4) (2021) 2877–2898.

[17] G. Habib, F. Romeo, The tuned bistable nonlinear energy sink, Nonlinear Dynamics 89 (1) (2017) 179–196.

[18] K. Dekemele, P. Van Torre, M. Loccufier, Performance and tuning of a chaotic bi-stable nes to mitigate transient vibrations, Nonlinear Dynamics 98 (2019) 1831–1851.

[19] K. Dekemele, G. Habib, Inverted resonance capture cascade: modal interactions of a nonlinear energy sink with softening stiffness, Nonlinear Dynamics.

[20] J. E. Chen, M. Sun, W. H. Hu, J. H. Zhang, Z. C. Wei, Performance of non-smooth nonlinear energy sink with descending stiffness, Nonlinear Dynamics 100 (2020) 255–267.

[21] K. Dekemele, G. Habib, M. Loccufier, The periodically extended stiffness nonlinear energy sink, Mechanical Systems and Signal Processing 169 (2022) 108706.

[22] W. Li, N. E. Wierschem, X. Li, T. Yang, M. J. Brennan, Numerical study of a symmetric single-sided vibro-impact nonlinear energy sink for rapid response reduction of a cantilever beam, Nonlinear Dynamics 100 (2020) 951–971.

[23] M. A. AL-Shudeifat, A. S. Saeed, Comparison of a modified vibro-impact nonlinear energy sink with other kinds of ness, Meccanica 56 (2021) 735–752.

[24] A. S. Saeed, R. Abdul Nasar, M. A. AL-Shudeifat, A review on nonlinear energy sinks: designs, analysis and applications of impact and rotary types, Nonlinear Dynamics (2022) 1–37.

[25] Y. S. Lee, A. F. Vakakis, L. A. Bergman, D. M. McFarland, G. Kerschen, Suppression aeroelastic instability using broadband passive targeted energy transfers, part 1: Theory, AIAA journal 45 (3) (2007) 693–711.

[26] Y. S. Lee, G. Kerschen, D. M. McFarland, W. J. Hill, C. Nichkawde, T. W. Strganac, L. A. Bergman, A. F. Vakakis, Suppressing aeroelastic instability using broadband passive targeted energy transfers, part 2: experiments, AIAA journal 45 (10) (2007) 2391–2400.

[27] O. V. Gendelman, A. F. Vakakis, L. A. Bergman, D. M. McFarland, Asymptotic analysis of passive nonlinear suppression of aeroelastic instabilities of a rigid wing in subsonic flow, SIAM Journal on Applied Mathematics 70 (5) (2010) 1655–1677.

[28] D. Andersen, Y. Starosvetsky, A. Vakakis, L. Bergman, Dynamic instabilities in coupled oscillators induced by geometrically nonlinear damping, Nonlinear Dynamics 67 (2012) 807–827.

[29] X. Kong, H. Li, C. Wu, Dynamics of 1-dof and 2-dof energy sink with geometrically nonlinear damping: application to vibration suppression, Nonlinear Dynamics 91 (2018) 733–754.

[30] Y. Liu, A. Mojahed, L. A. Bergman, A. F. Vakakis, A new way to introduce geometrically nonlinear stiffness and damping with an application to vibration suppression, Nonlinear Dynamics 96 (2019) 1819–1845.

[31] Y. Zhang, X. Kong, C. Yue, H. Xiong, Dynamic analysis of 1-dof and 2-dof nonlinear energy sink with geometrically nonlinear damping and combined stiffness, Nonlinear Dynamics 105 (1) (2021) 167–190.

[32] Y. Starosvetsky, O. Gendelman, Vibration absorption in systems with a nonlinear energy sink: nonlinear damping, Journal of Sound and Vibration 324 (3-5) (2009) 916–939.

[33] G. Habib, G. I. Cirillo, G. Kerschen, Isolated resonances and nonlinear damping, Nonlinear Dynamics 93 (2018) 979–994.

[34] H. Zuo, S. Zhu, Bistable track nonlinear energy sinks with nonlinear viscous damping for impulsive and seismic control of frame structures, Engineering Structures 272 (2022) 114982.

[35] Y. Zhang, X. Kong, C. Yue, Vibration analysis of a new nonlinear energy sink under impulsive load and harmonic excitation, Communications in Nonlinear Science and Numerical Simulation 116 (2023) 106837.

[36] T. Roncen, G. Michon, V. Manet, Design and experimental analysis of a pneumatic nonlinear energy sink, Mechanical Systems and Signal Processing 190 (2023) 110088.

[37] Z. Wu, S. Seguy, M. Paredes, Estimation of energy pumping time in bistable nonlinear energy sink and experimental validation, Journal of Vibration and Acoustics 144 (5) (2022) 051004.

[38] Z. Wu, S. Seguy, M. Paredes, Qualitative analysis of the response regimes and triggering mechanism of bistable nes, Nonlinear Dynamics 109 (2) (2022) 323–352.

[39] Y. Chen, W. Su, S. Tesfamariam, Z. Qian, W. Zhao, Z. Yang, F. Zhou, Experimental study of magnetic bistable nonlinear energy sink for structural seismic control, Soil Dynamics and Earthquake Engineering 164 (2023) 107572.

[40] X. Geng, H. Ding, X. Jing, X. Mao, K. Wei, L. Chen, Dynamic design of a magnetic-enhanced nonlinear energy sink, Mechanical Systems and Signal Processing 185 (2023) 109813.

[41] K. Dekemele, P. Van Torre, M. Loccufier, Design, construction and experimental performance of a nonlinear energy sink in mitigating multi-modal vibrations, Journal of Sound and Vibration 473 (2020) 115243.

[42] D. Zou, G. Liu, Z. Rao, T. Tan, W. Zhang, W.-H. Liao, A device capable of customizing nonlinear forces for vibration energy harvesting, vibration isolation, and nonlinear energy sink, Mechanical Systems and Signal Processing 147 (2021) 107101.

[43] D. Zou, K. Chen, Z. Rao, J. Cao, W.-H. Liao, Design of a quad-stable piezoelectric energy harvester capable of programming the coordinates of equilibrium points, Nonlinear Dynamics 108 (2) (2022) 857–871.

[44] L. Manevitch, The description of localized normal modes in a chain of nonlinear coupled oscillators using complex variables, Nonlinear Dynamics 25 (2001) 95–109.

[45] M. Urabe, Galerkin's procedure for nonlinear periodic systems, Tech. rep., WISCONSIN UNIV MADISON MATHEMATICS RESEARCH CENTER (1964).

[46] S. Karkar, B. Cochelin, C. Vergez, A comparative study of the harmonic balance method and the orthogonal collocation method on stiff nonlinear systems, Journal of Sound and Vibration 333 (12) (2014) 2554–2567.

[47] O. V. Gendelman, Targeted energy transfer in systems with non-polynomial nonlinearity, Journal of Sound and Vibration 315 (3) (2008) 732–745.

[48] K. Dekemele, Performance measures for nonlinear energy sinks in mitigating single and multi-mode vibrations: theory, simulation and implementation, Ph.D. thesis, Ghent University (2021).

Appendix A. Integrals

Appendix A.1. Nonlinear stiffness

To compute the integral (21), it is assumed that B is constant over the single period of integration, $Be^{i\tau} + B^* e^{-i\tau} = b\cos(\tau + \beta)$. Furthermore, the variable of integration is substituted by $\tau_\beta = \tau + \beta$. The integral in (21) where $f_\mathrm{s} = \gamma z^3 - \kappa z$ then is:

$$\begin{aligned} BG(|B|) &= \frac{1}{2\pi}\int_0^{2\pi} f_\mathrm{s}\left(Be^{i\tau} + B^* e^{-i\tau}\right) e^{-i\tau} d\tau \\ &= \frac{be^{i\beta}}{2\pi}\int_0^{2\pi}\left(\gamma b^2 \cos^3(\tau_\beta) - \kappa\cos(\tau_\beta)\right) e^{-i\tau_\beta} d\tau_\beta \\ &= \frac{b}{2}e^{i\beta}\left(\frac{3\gamma}{4}b^2 - \kappa\right) = B\left(3\gamma|B|^2 - \kappa\right) \end{aligned} \tag{A.1}$$

as such, $G(|B|) = 3\gamma|B|^2 - \kappa$, $G(b) = \frac{3\gamma}{4}b^2 - \kappa$ or $G(Z_b) = \frac{3}{4}Z_b - \kappa$.

Appendix A.2. Nonlinear geometric damping

The nonlinear geometric damping $c_\mathrm{gd}(z)$ obtained from (6) is even, which allows some simplification of the integral:

$$\begin{aligned} BH(|B|) &= \frac{1}{2\pi}\int_0^{2\pi} c_\mathrm{gd}\left(Be^{i\tau} + B^* e^{-i\tau}\right)\left(Be^{i\tau} - B^* e^{-i\tau}\right) e^{-i\tau} d\tau \\ &= \frac{be^{i\beta}}{2\pi}\int_0^{2\pi} c_\mathrm{gd}\left(\cos(\tau_\beta)\right)\sin^2(\tau_\beta) d\tau_\beta \end{aligned} \tag{A.2}$$

For $c_\mathrm{gd} = \tilde{\xi}_\mathrm{gd}\gamma z^2$:

$$\begin{aligned} BH(|B|) &= \tilde{\xi}_\mathrm{gd}\gamma\frac{b^3 e^{i\beta}}{2\pi}\int_0^{2\pi}\cos^2(\tau_\beta)\sin^2(\tau_\beta) d\tau_\beta \\ &= \tilde{\xi}_\mathrm{gd}\gamma\frac{b^3 e^{i\beta}}{8} = \tilde{\xi}_\mathrm{gd}\gamma B|B|^2 \end{aligned} \tag{A.3}$$

or , $H(|B|) = \tilde{\xi}_\mathrm{gd}\gamma|B|^2$ and $H(b) = \tilde{\xi}_\mathrm{gd}\gamma\frac{b^2}{4}$. For $c_\mathrm{gd} = \tilde{\xi}_\mathrm{gd}\gamma z^2 \frac{\left(\gamma z^2 - \kappa\right)^2}{\frac{\gamma^2}{4}z^4 - \frac{\kappa\gamma}{2}z^2 + \tilde{f}(0)^2}$:

$$
\begin{aligned}
&BH(|B|)\\
&=\tilde{\xi}_{\text{gd}}\gamma\frac{b^3e^{i\beta}}{8\pi}\int_0^{2\pi}\frac{\left(\gamma b^2\cos^2(\tau_\beta)-\kappa\right)^2}{\frac{\gamma^2}{4}b^4\cos^4(\tau_\beta)-\frac{\kappa\gamma}{2}b^2\cos^2(\tau_\beta)+\tilde{f}(0)^2}\sin^2(2\tau_\beta)d\tau_\beta\\
&=\tilde{\xi}_{\text{gd}}\gamma B\frac{|B|^2}{8\pi}\int_0^{2\pi}\frac{\left(\gamma|B|^2\cos^2(\tau_\beta)-\kappa\right)^2}{\frac{\gamma^2}{4}|B|^4\cos^4(\tau_\beta)-\frac{\kappa\gamma}{2}|B|^2\cos^2(\tau_\beta)+\tilde{f}(0)^2}\sin^2(2\tau_\beta)d\tau_\beta
\end{aligned}
\tag{A.4}
$$

or

$$
\begin{aligned}
&H(Z_b)\\
&= \quad =\tilde{\xi}_{\text{gd}}\frac{Z_b}{8\pi}\int_0^{2\pi}\frac{\left(\gamma Z_b\cos^2(\tau_\beta)-\kappa\right)^2}{\frac{Z_b^2}{4}\cos^4(\tau_\beta)-\frac{\kappa Z_b}{2}\cos^2(\tau_\beta)+\tilde{f}(0)^2}\sin^2(2\tau_\beta)d\tau_\beta
\end{aligned}
\tag{A.5}
$$

The integral cannot be further evaluated analytically, but is easily approximately solved through a Taylor series approximation or is easily computed numerically.

Appendix B. Stability of SIM

The stability of the solutions on the SIM are computed with the 2nd equation of (23). Linearizing this equation around equilibrium $B_{\text{eq}}=\frac{b}{2}e^{\beta}$ obtained from the solutions of (24) gives the following set of equations:

$$
\begin{bmatrix}\dot{\Delta}_B\\ \dot{\Delta}_B^*\end{bmatrix}=\underbrace{\begin{bmatrix}a_{11} & a_{12}\\ a_{21} & a_{22}\end{bmatrix}}_{\mathbf{\Sigma}}\begin{bmatrix}\Delta_B\\ \Delta_B^*\end{bmatrix}
\tag{B.1}
$$

where $\Delta_B=B-B_{\text{eq}}$ and

$$
\begin{aligned}
a_{11}=a_{22}^*&=-\frac{i}{2}-\frac{\xi_{na}}{2}+\frac{i}{2}\left.\frac{\partial(B\cdot G(B,B^*))}{\partial B}\right|_{B=B_{\text{eq}}}-\frac{1}{2}\left.\frac{\partial(B\cdot H(B,B^*))}{\partial B}\right|_{B=B_{\text{eq}}}\\
a_{12}=a_{21}^*&=\frac{i}{2}\left.\frac{\partial(B\cdot G(B,B^*))}{\partial B^*}\right|_{B=B_{\text{eq}}}-\frac{1}{2}\left.\frac{\partial(B\cdot H(B,B^*))}{\partial B^*}\right|_{B=B_{\text{eq}}}
\end{aligned}
\tag{B.2}
$$

Finally, the stability is determined by computing the eigenvalues of $\mathbf{\Sigma}$ matrix in (C.1). If any eigenvalue has a positive real part, the solution is unstable.

Appendix C. Stability under harmonic load

The stability of the harmonic balanced solution (45) is computed from the linear stability around equilibrium of A and B:

$$2i\sqrt{X}\begin{bmatrix}\dot{\Delta}_A\\ \dot{\Delta}_A^*\\ \dot{\Delta}_B\\ \dot{\Delta}_B^*\end{bmatrix}=\underbrace{\begin{bmatrix}a_{11}&a_{12}&a_{13}&a_{14}\\ a_{21}&a_{22}&a_{23}&a_{24}\\ a_{31}&a_{32}&a_{33}&a_{34}\\ a_{41}&a_{42}&a_{43}&a_{44}\end{bmatrix}}_{\boldsymbol{\Sigma}}\begin{bmatrix}\Delta_A\\ \Delta_A^*\\ \Delta_B\\ \Delta_B^*\end{bmatrix} \tag{C.1}$$

where $\Delta_A = A - A_{\text{eq}}$, $\Delta_B = B - B_{\text{eq}}$ and

$$\begin{aligned}
&a_{12} = a_{21} = a_{32} = a_{41}\\
&a_{11} = -a_{22}^* = -\varepsilon\sigma - i\varepsilon\xi\sqrt{X}\\
&a_{13} = -a_{24}^* = i\varepsilon\xi_{na}\sqrt{X} + \varepsilon\left.\frac{\partial(B\cdot G(B,B^*))}{\partial B}\right|_{B=B_{\text{eq}}} + i\varepsilon\sqrt{X}\tilde{\xi}_{\text{gd}}\left.\frac{\partial(B\cdot\tilde{H}(B,B^*))}{\partial B}\right|_{B=B_{\text{eq}}}\\
&a_{14} = -a_{23}^* = \varepsilon\left.\frac{\partial(B\cdot G(B,B^*))}{\partial B^*}\right|_{B=B_{\text{eq}}} + i\varepsilon\sqrt{X}\;\tilde{\xi}_{\text{gd}}\left.\frac{\partial(B\cdot\tilde{H}(B,B^*))}{\partial B^*}\right|_{B=B_{\text{eq}}}\\
&a_{31} = -a_{42}^* = \varepsilon\sigma + i\varepsilon\xi\sqrt{X} + X\\
&a_{33} = -a_{44}^* = X - \frac{1+\varepsilon}{\varepsilon}a_{13}\\
&a_{34} = -a_{43}^* = -\frac{1+\varepsilon}{\varepsilon}a_{14}
\end{aligned} \tag{C.2}$$

The stability is then determined from the eigenvalues of $\frac{\boldsymbol{\Sigma}}{2i\sqrt{X}}$.